

Inhibiting inflammation in adipocytes accelerates mammary tumor development in mice

Dae-Seok Kim¹, Toshiharu Onodera^{1,2}, Jan-Bernd Funcke¹, Kyounghee Min¹, Qingzhang Zhu¹,
Qian Lin, Shihwei Chen¹, Chanmin Joung¹, Min Kim³, R. Max Wynn¹, Joselin Velasco¹,
Charlotte Lee⁴, Megan Virostek¹, Chao Li¹, Philipp E. Scherer^{1,*}

5

¹ Touchstone Diabetes Center, The University of Texas Southwestern Medical Center, Dallas, TX,
United States

² Department of Adipose Management, Osaka University Graduate School of Medicine, Osaka,
Japan

10 ³ Department of Biological Sciences, School of Life Sciences, Ulsan National Institute of Science
and Technology, Ulsan, South Korea

⁴ Center for Hypothalamic Research, Department of Internal Medicine, The University of Texas
Southwestern Medical Center, Dallas, TX, United States

15

* Corresponding author: Philipp E Scherer, Ph.D.

Touchstone Diabetes Center, The University of Texas Southwestern Medical Center, Dallas,
United States.

E-mail : Philipp.Scherer@UTSouthwestern.edu

20 Tel : +1-214-648-8715 Fax : (214) 648-8720

Authorship notes: D-SK and TO are co-first authors and contributed equally to this work.

Conflict of interest: The authors have declared that no conflict of interest exists.

25

Abstract

Pro-inflammatory signaling in adipocytes is essential for healthy adipose expansion, remodeling, and tissue integrity. We investigated the effects of targeting inflammation in either adipocytes or mammary gland epithelial cells, in the context of mammary tumor development, by locally
30 expressing the anti-inflammatory adenoviral RID α/β protein complex in a cell type-specific manner. Suppression of adipocyte inflammation ("RID^{ad} mice") in a mammary tumor model driven by MMTV-PyMT ("PyMT-RID^{ad} mice") led to an elevated number of tumor-associated macrophages (TAMs) and upregulation of immunoregulatory molecules in the mammary fat pad (MFP). This was accompanied by metabolic dysfunction and abnormal mammary gland development.
35 Importantly, this phenotype correlated with accelerated mammary tumor onset, enhanced growth, and lung metastasis. Tumors in PyMT-RID^{ad} mice exhibited upregulated CD36 expression, suggesting enhanced fatty acid uptake. Conversely, suppression of inflammation in mammary gland epithelial cells by RID α/β expression ("RID^{MMTV} mice") decelerated mammary tumor growth without affecting tumor onset or macrophage accumulation. These findings highlight the
40 differential impact on tumor development exerted through the suppression of inflammatory signals in different cell types in the microenvironment. Our results underscore the role of the suppression of adipocyte inflammation leading to a tumor-friendly microenvironment, promoting mammary cancer progression. This study sheds light on the complex interplay between inflammation, specifically driven by the adipocyte, in breast cancer pathogenesis.

Keywords:

RID α/β , Inflammation, Adipose tissue, Mammary fat pad, Tumor-associated macrophages (TAMs), Breast cancer.

Introduction

Our previous studies focused on the pathophysiological effects of an impaired local pro-inflammatory response within adipocytes (1). This led to increased ectopic lipid accumulation, glucose intolerance, and systemic inflammation (1). These findings came as a surprise at the time, since there was a general belief that inflammation in adipose tissue is an integral part of the metabolic syndrome, and anti-inflammatory actions were thought to lead to metabolic improvements. However, our findings suggested that pro-inflammatory signaling in the adipocyte is, in fact, required for proper adipose tissue remodeling and expansion. These findings not only deepened our overall understanding of adipose tissue dynamics in relation to inflammation but also established an approach to effectively intervene in the inflammatory process by targeted overexpression of the adenoviral receptor internalization and degradation protein complex, RID α / β . Previous studies indicated that RID α / β represents a transmembrane heterotrimeric complex comprising 10.4 kDa and 14.5 kDa subunits encoded by the adenovirus E3 region (2-6). This complex has been reported to robustly suppress key inflammatory pathways *in vitro*, including those involving LPS/TLR4, TNF α /TNFR, and IL1 β /IL1R (2-4). Importantly, our recent study employing adipocyte-specific doxycycline (Dox)-inducible RID α / β transgenic mice (RID^{ad}) demonstrated that suppressing inflammatory pathways in adipocytes directly impacts metabolic outcomes (7). Despite a reduced weight gain, RID^{ad} mice exhibited exacerbated metabolic dysfunction, including glucose intolerance and insulin resistance, fatty liver, and reduced adiponectin levels. Consistent with previous reports (2, 3), a significant reduction in pro-inflammatory factors was observed, particularly notable was a reduction in M1-like macrophage markers such as *Tnf*, *Il1b*, and *Saa3*. Intriguingly, alongside this reduction, an increase in *Adgre1* expression was noted. This was accompanied by elevated levels of M2-like macrophage markers such as *Mgl1*, *Mrc1*, and *Clec10a*. These findings suggest that RID α / β induces macrophage polarization toward an M2-like phenotype in adipose tissue through the regulation of inflammation. Numerous studies have underscored the intricate interplay between inflammatory processes and

their profound impact on the initiation, progression, and metastasis of cancer (8, 9). A growing body of evidence has highlighted the important role played by chronic inflammation within the mammary environment, implicating that it creates a favorable setting for the growth and advancement of breast tumors (10-14). Furthermore, inflammatory signaling pathways have been identified as critical regulators of tumor-promoting processes, influencing aspects such as cell proliferation, angiogenesis, and immune evasion (9, 14, 15). Recent studies have explored this further, revealing details about specific molecular pathways connecting inflammation to the development of breast tumors (16, 17). Such findings highlight the crucial role of inflammatory signaling in shaping the tumor microenvironment. Despite these insights, a comprehensive examination of the tissue-specific regulation of inflammation, especially within adipocytes and tumor cells, and its implications for mammary tumor development has not been done to date in detail. Additionally, the unresolved question persists as to whether the expansion of dysfunctional adipose tissues during a high-fat diet (HFD) challenge, resulting from the suppression of inflammation in adipocytes, exerts relevant effects on the initiation and progression of mammary tumors. Our previous studies were focused on unraveling the profound connections between RID α/β -mediated inflammation modulation and its extensive impact on metabolic regulation (1, 7).

In this study, we investigated how a selective RID α/β -mediated suppression of inflammation in either adipocytes or mammary gland epithelial cells (*i.e.*, the cells from which the tumor stems) impacts the intricate landscape of tumorigenesis within the mammary microenvironment. To this end, we utilized RID^{ad} mice (7), in which adipocyte inflammation is suppressed, and transplanted them with mouse breast cancer cells. We also generated a transgenic model of breast cancer development in the presence of suppressed adipocyte inflammation, PyMT-RID^{ad}, by combining the RID^{ad} model with mammary gland epithelial cell-specific expression of the polyomavirus middle T antigen (PyMT) (18, 19). Additionally, we created another transgenic model, PyMT-RID^{MMTV}, in which both RID α/β and PyMT are expressed

specifically in mammary gland epithelial cells, allowing us to assess breast cancer development under conditions of suppressed mammary gland epithelial cell inflammation. Using these genetic mouse models, we demonstrate that suppression of adipocyte inflammation leads to adipocyte apoptosis, metabolic alternation, and recruitment of tumor-associated macrophages (TAMs), collectively contributing to an immune-suppressive, tumor-promoting microenvironment. In contrast, suppression of inflammation in mammary gland epithelial cells in PyMT-RID^{MMTV} mice results in decelerated tumor growth without affecting tumor onset or TAMs accumulation.

110 **Results**

RID α / β and inflammatory gene expression in RID^{ad} mice

Our previous findings characterized the metabolic consequences of inflammation suppression in adipocytes using the Dox-inducible RID^{ad} mouse model (Figure 1A) (7). Here we utilized the RID^{ad} model to investigate how modulating the inflammatory process in adipocytes contributes to breast tumor development. We first validated cell type-specific RID α / β expression using a range of assays. Quantitative PCR (qPCR) analysis demonstrated robust RID α / β induction in the mammary fat pad (MFP) (Figure 1B) and in the gonadal white adipose tissue (gWAT) (Figure 1C) following a 12-week challenge with a Dox-containing HFD. Western blotting confirmed the expression of RID β in both adipose depots (Figure 1D). Of note, while we generated distinct antibodies against RID α and RID β , the RID α antibody displayed an unacceptable level of background signal and was thus not used (data not shown). RID β expression was not detectable in the liver, supporting the intended restriction of transgene expression to adipocytes (Figure 1D). Immunostaining of the MFP and gWAT, particularly co-staining with perilipin and RID β antibodies, further confirmed the adipocyte-selective induction of RID α / β within adipose tissue (Figure 1E and F). Importantly, RID β expression was not detected in mammary gland epithelial cells (Figure 1E and Supplemental Figure 1A; detailed images). In our previous study, male RID^{ad} mice exhibited a significant decrease in the expression of pro-inflammatory genes such as *Tnf* and *Il1b* (7). In contrast, female mice subjected to a long-term Dox-HFD regimen of 12 weeks, which is the focus of our study here, exhibited an upregulation of multiple inflammation-related genes in the MFP (Figure 1G) and gWAT (Figure 1H). However, this effect was mitigated in isolated adipocytes from the MFP (Supplemental Figure 1B and C), suggesting that the overall induction of inflammatory genes within adipose tissue of female mice arises from other cell types, such as mammary gland epithelial cells or infiltrating immune cells, rather than from adipocytes. Notably, *Ccl2*, known for its high expression within the tumor microenvironment and its pivotal role in recruiting TAMs (20), which generally resemble M2-like macrophages, was significantly upregulated in both the MFP

and gWAT (Figure 1G and H). In line with this, RID^{ad} mice displayed an upregulation of M2 macrophage-related genes, including *Arg1* in both MFP and gWAT as well as *Mgl1* in gWAT. Furthermore, the pan-macrophage marker gene *Adgre1* was significantly upregulated in both the MFP and gWAT, suggesting macrophage accumulation and M2 polarization in response to prolonged suppression of adipocyte pro-inflammatory signaling in female mice. These results are consistent with our previous findings that macrophages in the adipose tissue of RID^{ad} mice are polarized toward an M2-like phenotype in adipose tissue (7). Collectively, these findings underscore the complex and sex-dependent nature of adipose tissue inflammation and highlight the potential impact of prolonged inflammation-modulating interventions on macrophage dynamics in females.

Increased adipocyte apoptosis and crown-like structure formation in RID^{ad} mice

Macrophage-related markers were significantly upregulated in the MFP and gWAT of RID^{ad} mice that were fed Dox-HFD (Figure 1G and H). We hypothesized that the suppression of pro-inflammatory signaling in adipocytes causes cell damage and unhealthy tissue expansion upon Dox-HFD challenge. This cell damage could result in increased apoptosis and subsequent recruitment of macrophages to remove cellular debris. To investigate this hypothesis, we performed immunostaining with antibodies for cleaved caspase-3 and perilipin to get a better sense of the degree of the apoptotic processes in the adipose tissues of RID^{ad} mice. Strikingly, cleaved caspase-3 was detectable at high frequency in adipocytes in the MFP (Figure 2A and B) as well as gWAT (Figure 2C and D) of RID^{ad} mice compared to control mice, indicating increased apoptosis. Western blotting analysis of the MFP for cleaved caspase-3 further supported this observation (Supplemental Figure 2A and B). Although gWAT also showed increased apoptosis, the difference was not statistically significant upon quantification (Supplemental Figure 2A and B). In adipose tissue, macrophages cluster around apoptotic adipocytes, forming crown-like structures (CLSs) (21, 22). Intriguingly, emerging evidence indicates that CLSs in adipose depots

such as the MFP, particularly in the context of obesity, are associated with the development and progression of breast cancer (23). As we observed an increase in macrophage-related markers and adipocyte apoptosis in the MFP of RID^{ad} mice (Figure 1, G and H), we sought to determine whether apoptotic signaling is associated with exacerbated macrophage accumulation and CLS formation in MFP and gWAT. We assessed CLS formation by immunostaining using a MAC-2 antibody, which revealed an increased accumulation of CLSs in the MFP (Figure 2E and G; Supplemental Figure 2C; detailed images) and gWAT (Figure 2F and G; Supplemental Figure 2C; detailed images) of RID^{ad} mice compared to control mice. The presence of CLSs was further confirmed by hematoxylin and eosin (H&E) staining (Supplemental figure 2D). Together, these observations suggest that the suppression of inflammation in MFP and gWAT during HFD challenge triggers adipocyte apoptosis, leading to the subsequent accumulation of macrophages in the MFP and gWAT of RID^{ad} mice. This dynamic interplay results in a fundamental change in the cellular composition within the microenvironment of the tissue.

175

Increased TAM accumulation and accelerated tumor growth in the MFP of RID^{ad} mice

The infiltration and accumulation of TAMs within the tumor microenvironment are pivotal for tumor progression (24-26). Notably, enhanced macrophage recruitment and accumulation, along with a significant upregulation of *Ccl2*, a key factor for TAM recruitment, were observed in the MFP and gWAT of RID^{ad} mice (Figures 1 and 2). Thus, we hypothesized that the increased presence of macrophages in the MFP and gWAT of RID^{ad} mice may also reflect a greater number of TAMs, even though these mice did not carry any tumors. To assess TAM recruitment and accumulation, immunostaining with a CD163 antibody, a TAM marker (27-30), was performed. CD163 expression was significantly higher in the MFP (Figure 3A and B) and gWAT (Figure 3C and D) of RID^{ad} mice compared to control mice, indicative of increased TAM presence. Expression of another well-established TAM marker, CD206, was significantly higher in the MFP of RID^{ad} mice compared to control mice as well, further supporting the increased presence of TAMs.

185

(Supplemental Figure 3A and B). To investigate the effects of suppressing adipocyte inflammation on tumor development, we employed a syngeneic breast cancer mouse model (Figure 3E).
190 EO771 cells were injected into the MFP of both control and RID^{ad} mice that were pre-fed with HFD and subsequently switched to Dox-HFD for induction of RID α/β expression. Notably, suppression of adipocyte inflammation significantly enhanced the growth of syngeneic tumors in RID^{ad} mice compared to control mice (Figure 3F-H), without affecting body weight (Figure 3I) or the composition or gross morphology of the MFP (Figure 3J and K). In line with this observation,
195 conditioned medium (CM) collected from *in vitro*-differentiated adipocytes of RID^{ad} mice promoted cancer cell proliferation and migration in several human breast cancer cell lines (Supplemental Figure 4A-C). Interestingly, CM from *in vitro*-differentiated adipocytes of RID^{ad} mice (C57BL/6 mice background) induced the proliferation and migration of EO771 cells (C57BL/6 mice-derived), but not MET1 cells (FVB mice-derived), suggesting a background-specific effect of CM
200 (Supplemental Figure 4D-F).

Earlier mammary tumor onset, accelerated tumor growth, and a higher incidence of lung metastasis in PyMT-RID^{ad} mice

To study an autochthonous model of breast cancer development, we generated PyMT-
205 RID^{ad} mice, which are RID^{ad} mice carrying the MMTV-PyMT transgene (Figure 4A). Female MMTV-PyMT spontaneously develop breast cancer, providing an ideal model for exploring the detailed outcomes of suppressing adipocyte inflammation (18). Our analysis focused on the MFP rather than gWAT, as breast tumor primary arises and progress in the MFP. First, examination of the MFP in PyMT-RID^{ad} mice fed Dox-HFD revealed abnormal mammary gland development
210 compared to PyMT mice, as determined by H&E staining (Figure 4B and Supplemental Figure 5A; magnified images). Second, PyMT-RID^{ad} mice showed a significantly earlier in mammary tumor onset, developing palpable tumors at a younger age than PyMT mice (Figure 4C). PyMT-RID^{ad} mice furthermore exhibited significantly faster in tumor growth compared to PyMT mice

(Figure 4D), without any effect on body weight (Figure 4E). Tumors isolated from each group confirmed that RID α/β overexpression in adipocytes promotes tumor growth (Figure 4F). Additionally, tumors from PyMT-RID^{ad} mice displayed a notable increase in actively proliferating, Ki67-positive tumor cells (Figure 4G and Supplemental Figure 5B and C). Also, the development of blood vessels within the tumor lesions compared to PyMT mice was enhanced, as indicated by CD31 staining and H&E staining (Figure 4H and I; Supplemental Figure 5D). These findings suggests that the suppression of inflammation in adipocytes stimulates both tumor development and growth. Interestingly, the number of macrophages at this late stage of tumor development was significantly decreased in the MFP of PyMT-RID^{ad} mice compared to PyMT mice, which contrasts with our observations in RID^{ad} mice (Supplemental Figure 5E-G). Increased nutritional competition between tumor cells and macrophages has been reported to limit macrophage survival and function in the tumor microenvironment (31-33). In PyMT-RID^{ad} mice, where the MFP exhibits extensive tumor development, such competition may account for the reduced macrophage presence observed under this condition. Additionally, tumors from PyMT-RID^{ad} mice expressed comparable levels of estrogen receptor α (ER α) compared to PyMT mice, indicating that the rapid tumor development and progression in PyMT-RID^{ad} mice occurs in an ER α -independent manner (Supplemental Figure 5H). Finally, examination of the lungs of PyMT-RID^{ad} mice revealed metastatic tumor development, a phenomenon not detectable in PyMT mice at this time point (Figure 4J). In conclusion, the suppression of inflammation in adipocytes in PyMT-RID^{ad} mice promotes an earlier mammary tumor onset, accelerates tumor growth, and fosters the formation lung metastases.

235

Metabolic dysfunction and increased lipid uptake in tumors of PyMT-RID^{ad} mice

Next, we performed RNA-seq to further elucidate the changes in tumor gene expression occurring in the context of suppressed adipocyte inflammation (Supplemental Figure 6A). Among the top five pathways identified in the RNA-seq analysis, the AMPK signaling pathway, known for

240 negatively regulating the mTOR pathway and thereby inhibiting cancer cell survival and proliferation, was significantly downregulated (Supplemental Figure 6B; top) (34). Although not among the top five, tumors from PyMT-RID^{ad} mice displayed a significant upregulation of Wnt and PI3K-Akt signaling pathways (Supplemental Figure 6B; bottom), which are critical regulators of tumor progression (35). Our RNA-seq findings thus partially explain the heightened proliferation and more aggressive tumor phenotype observed in PyMT-RID^{ad} mice. Given that highly proliferative tumors require increased fatty acid uptake to support their growth, we next hypothesized that genes involved in fatty acid metabolism would be upregulated in tumors from PyMT-RID^{ad} mice. To test this hypothesis, we examined the protein expression of key factors involved in fatty acid uptake and metabolism, including CD36 and FABP4, in tumor tissues by immunostaining. We found that CD36 is highly expressed in tumors from PyMT-RID^{ad} mice compared to PyMT mice (Figure 5A and Supplemental Figure 7; different area). FABP4 displayed a slightly higher expression in PyMT-RID^{ad} tumors as well (Figure 5B). CD36 plays a critical role in lipid metabolism by facilitating the uptake of free fatty acids. These results suggest that the tumors in PyMT-RID^{ad} mice may rely on fatty acids to support their growth. To test whether interference with CD36 blocks tumor cell proliferation in PyMT-RID^{ad} mice, we isolated tumor cells from PyMT and PyMT-RID^{ad} mice and cultured them *in vitro* (Supplemental Figure 8A). The tumor cells formed colonies at passage 0 in both groups, and after passaging, tumor cells from PyMT mice exhibited poor colonies formation, whereas those from PyMT-RID^{ad} mice appeared to form colonies well (Supplemental Figure 8B, passage 2). Therefore, we only performed further experiments using tumor cells from PyMT-RID^{ad} mice. Treatment with the CD36 inhibitor Sulfosuccinimidyl Oleate (SSO) slightly reduced tumor cell proliferation when used at higher concentrations, suggesting that tumor cells from PyMT-RID^{ad} mice appear to rely on CD36 expression on their surface (Supplemental Figure 8C). To further elucidate changes in systemic and local metabolism in PyMT-RID^{ad} mice, we conducted a comprehensive evaluation of metabolic parameters, including systemic glucose tolerance, insulin sensitivity, lipid clearance,

245
250
255
260
265

and triolein uptake, while monitoring tumor development (Figure 5C). We found that PyMT-RID^{ad} mice exhibited systemic metabolic dysfunction, including mild glucose intolerance (Figure 5D) and moderate insulin resistance (Figure 5E) compared to PyMT mice. To assess lipid clearance in these animals, we performed oral triglyceride (TG) challenges (Supplemental Figure 9). The 270 fasting plasma TG and free fatty acid (FFA) levels were comparable between PyMT and PyMT-RID^{ad} mice, suggesting that systemic lipid metabolism was not altered. However, a triolein uptake experiment revealed that the tumors took up a significantly higher amount of triolein (Figure 5F), while the MFP itself displayed a lower triolein uptake in PyMT-RID^{ad} mice (Figure 5G). These observations suggest that metabolically dysfunctional adipocytes in the MFP of PyMT-RID^{ad} mice 275 have a reduced ability to take up and metabolize lipids, whereas the tumor lesions show a greater ability to do so. This aligns well with our observations of the highly proliferative character of the tumors in PyMT-RID^{ad} mice (Figure 4 and Supplemental Figure 10), as shown by their high expression of CD36 (Figure 5A). Other tissues, including gWAT (Figure 5H) and the liver (Figure 5I), did not show significant changes in triolein uptake, corroborating the functional and direct 280 interaction between the mammary adipocytes and tumor cells. Taken together, our data indicate that the metabolically dysfunctional mammary environment in PyMT-RID^{ad} mice promotes the development of highly proliferative tumors that show an elevated capacity of fatty acid uptake.

Increased CLS formation and TAM accumulation at early stages of tumor development in 285 PyMT-RID^{ad} mice

Following 12 weeks of Dox-HFD feeding, the MFP in PyMT-RID^{ad} mice displayed a notable proliferation of mammary gland tissue and the emergence of tumors (Figure 4B). This proliferation significantly altered the accumulation of macrophages within the MFP (Supplemental Figure 5E). Furthermore, the widespread presence of actively proliferating mammary gland components and 290 tumor cells within the MFP posed challenges for obtaining pure adipose samples suitable for RNA sequencing. Therefore, we investigated the early-stage tumor-associated pathological changes

in PyMT-RID^{ad} mice following a short-term Dox-HFD challenge of only 4 weeks to identify potential factors that could stimulate rapid tumor growth while avoiding the confounding effects of tumor contamination observed at the 12-week stage. First, we observed that the abdominal MFP in
295 PyMT-RID^{ad} mice already showed slightly proliferative mammary gland epithelial cells and early tumor development compared to PyMT mice (Figure 6A, left), while the inguinal MFP showed barely detectable mammary gland proliferation and tumor development (Figure 6A, right). Additionally, immunostaining for Ki67 revealed a moderate number of proliferating tumor cells in the abdominal MFP, while only a small number were detected in the inguinal MFP, indicating
300 significantly lower tumor cell contamination in the inguinal MFP (Figure 6B and Supplemental Figure 11; detailed images). These observations suggest that a short-term HFD challenge of 4 weeks serves as an effective model for investigating early dynamic changes in the MFP preceding the onset of highly proliferative mammary glands and mammary tumor development. To this end, we collected one side of the entire MFP for analysis of CLS formation, TAM recruitment, and
305 expression of cleaved caspase-3. To assess CLS formation, we conducted MAC-2 immunostaining, which revealed an increased abundance of MAC-2-positive cells forming CLSs in the MFP of PyMT-RID^{ad} mice compared to PyMT mice (Figure 6C and D; Supplemental Figure 12; detailed images). Additionally, to assess TAM recruitment and accumulation, CD163 and CD206 immunostainings were carried out. Expression of both CD163 (Figure 6E and F) and
310 CD206 (Supplemental Figure 13) were significantly higher in the MFP of PyMT-RID^{ad} mice compared to PyMT mice. Interestingly, CD163-positive cells were highly enriched in the proximal region from the tumor compared to distal regions, indicative of an increased number of TAMs more closely located near the tumor lesions (Figure 6E). Importantly, we observed recruitment of TAMs in the MFPs of both groups of mice, *i.e.* with and without tumor lesions (RID^{ad} in Figure 3A and PyMT-RID^{ad} in Figure 6E), reflecting an overall tumor-favorable environment and suggesting
315 that TAM recruitment may be a critical factor in stimulating tumor growth in our mouse model. However, we did not observe an enhanced induction of apoptosis at this earlier stage, as indicated

by the lack of signal for cleaved caspase-3 in PyMT-RID^{ad} mice (data not shown). Macrophages within adipose tissue aggregate to form CLS around adipocytes undergoing apoptosis (22).
320 Despite the absence of cleaved caspase-3, we observed a significant increase in CLSs during the short-term HFD challenge in PyMT-RID^{ad} mice, suggesting that adipocytes in these mice may undergo apoptosis at higher rates, resulting in an increased recruitment of macrophages (Figure 6C and D).

325 **Inflammation suppression in adipocytes alters the tumor microenvironment, metabolism, and immune landscape in PyMT-RID^{ad} mice**

To understand how early alterations of the MFP in PyMT-RID^{ad} mice contribute to the acceleration of mammary tumor development and progression, we performed RNA-seq on the MFP of PyMT-RID^{ad} and PyMT mice fed Dox-HFD for only 4 weeks (Supplemental Figure 14). Furthermore, due
330 to the relatively lower contamination of the inguinal MFP with tumor cells, we utilized that portion of the MFP for our analysis (Figure 6A and B; Supplemental Figure 14). RNA-seq revealed that the suppression of inflammation in adipocytes altered the expression of hundreds of genes in PyMT-RID^{ad} mice compared to PyMT mice (Figure 7A and Supplemental Figure 14). Initially, we observed that multiple TAM-related genes, including *Cd68*, *Cd163*, and *Mrc1*, but not *Msr1*, were
335 highly upregulated in PyMT-RID^{ad} mice (Figure 7B). This finding aligns well with our histological observations (Figure 6E) and highlights the recruitment and accumulation of TAMs in the MFP of PyMT-RID^{ad} mice. This phenomenon represents one of the most prominent consequences of inflammation suppression in adipocytes in our model. Importantly, the MFP of PyMT-RID^{ad} mice also exhibited an enrichment of immunoregulatory molecules such as *Ido1*, *Mrc1*, and *Cd200*,
340 suggesting a shift toward a generally immunosuppressive tumor microenvironment (Figure 7C). The upregulation of *Mrc1* implies an increase in pro-tumorigenic M2 macrophages (36) and elevated *Cd200* expression may contribute to immune evasion by inhibiting anti-tumor immune responses (37). *Ido1* in turn is known to facilitate tumor immune escape by suppressing T cell

activity and promoting regulatory T cell (Treg) expansion (38-40). Immunostaining confirmed significantly higher IDO1 expression in both mammary gland epithelial cells and tumor cells in PyMT-RID^{ad} mice compared to PyMT controls (Figure 7D and Supplemental Figure 15; detailed images). Despite these immunosuppressive changes, we did not observe any detectable differences in M1 macrophages, dendritic cells, NK cells, or T cells in the MFP of RID^{ad} mice (Supplemental Figure 16) and PyMT-RID^{ad} mice (Supplemental Figure 17) when compared to their respective controls. These findings suggest that RID^{ad} promotes an immunosuppressive tumor microenvironment through an upregulation of IDO1 in yet to be identified cell types as well as an augmented recruitment of immunomodulatory TAMs, rather than through direct alterations in other immune cell populations. We indeed observed an upregulation of multiple chemokines in the MFP of PyMT-RID^{ad} mice that may facilitate macrophage recruitment (Figure 7E). Apoptosis-related genes were also highly enriched in the MFP of PyMT-RID^{ad} (Figure 7F and Supplemental Figure 18), supporting our hypothesis that inflammation suppression by RID α/β overexpression induces increased adipocyte apoptosis. Furthermore, genes related to mammary gland development, mammary duct morphogenesis, tumor progression, and metastasis were significantly upregulated in the MFP of PyMT-RID^{ad} mice, consistent with histological evidence of highly proliferative mammary glands (Supplemental Figure 19A and B). In contrast, many genes involved in glycolysis, glycogen metabolism, and browning were downregulated following inflammation suppression in adipocytes (Supplemental Figure 19A and B). This reduction in glycolytic activity may increase nutrient availability within the tumor microenvironment, thereby facilitating tumorigenesis. Interestingly, *I12a*, a critical regulator of inflammation, (41) was significantly downregulated in the MFP of PyMT-RID^{ad} mice (Supplemental Figure 19C). This suggests that *I12a* may be one of the main targets affected by RID α/β overexpression, leading to the suppression of inflammation. Subsequent pathway analysis (Supplemental Figure 20) revealed impaired insulin signaling in the MFP of PyMT-RID^{ad}, marked by downregulation of the PI3K-Akt pathway (Supplemental Figure 20C), further linking RID α/β overexpression to insulin

370 resistance. Intriguingly, RID^{ad} mice without PyMT subjected to 12 weeks of Dox-HFD feeding showed increased adipocyte size (Supplemental Figure 21A). Similarly, at 4 weeks in PyMT-RID^{ad} mice, prior to tumor development, adipocyte hypertrophy was evident as well (Supplemental Figure 21B). This suggests that adipocyte enlargement may be at the root of diminished insulin signaling in the MFP of PyMT-RID^{ad} mice (42). These findings suggest that impaired insulin
375 signaling and metabolic dysfunction precede and promote tumor development. Interestingly, at 12 weeks, when PyMT-RID^{ad} mice exhibit a tumor burden, overall adipocyte size remained unchanged when randomly assessed (Supplemental Figure 21C). However, adipocytes adjacent to tumors appeared smaller, likely due to increased lipolysis and metabolic demand within the tumor microenvironment (Supplemental Figure 21D). These opposing effects, RID α/β -induced
380 hypertrophy versus tumor-driven adipocyte reduction, may offset one another, explaining the lack of a significant difference in overall adipocyte size. Collectively, these findings demonstrate that suppression of inflammation in adipocytes profoundly reprograms the metabolic and immune landscape of the MFP, promoting an immunosuppressive tissue microenvironment that benefits tumor development and growth.

385

Decelerated mammary tumor growth but unchanged tumor onset and tissue macrophage accumulation in PyMT-RID^{MMTV} mice

Pro-inflammatory factors, such as TNF- α , IL-1 β , and IL6 influence the development and progression of mammary tumors (8, 14). Chronic inflammation has been linked to increased
390 breast cancer development, contributing to the processes of initiation, promotion, and metastasis of tumors (8, 14). We observed that the suppression of inflammation in adipocytes significantly increased breast tumor onset, growth, and metastasis (Figure 4). These observations indicate that the inhibition of inflammation in different tissues may have distinct effects on breast tumor development and progression. To explore the specific tumor-associated pathological outcomes
395 of a suppression of inflammation in mammary gland epithelial cells, we generated mammary

gland epithelial cell-specific, Dox-inducible RID α/β -transgenic mice and bred them into the MMTV-PyMT mammary tumor model, resulting in PyMT-RID^{MMTV} mice (Figure 8A). Immunostaining of the MFP with RID β and perilipin antibodies highlighted the mammary gland epithelial cell-specific expression of RID β in these mice (Figure 8B and Supplemental Figure 22; 400 detailed images). This was evident with no detectable expression of RID β in adipocytes. Due to the limitations of the RID β antibody, which is a rabbit polyclonal antiserum, there was a slight background signal for RID β in mammary gland epithelial cells of PyMT mice. However, a much higher RID β signal was observed in such cells in PyMT-RID^{MMTV} mice (Figure 8B). We found that abnormal mammary gland development was significantly reduced in PyMT-RID^{MMTV} mice 405 compared to PyMT mice, contrasting our observations in PyMT-RID^{ad} mice (Figure 8C and Supplemental Figure 23; additional images). Additionally, PyMT-RID^{MMTV} mice exhibited a comparable mammary tumor onset, developing palpable tumors around the same time as PyMT mice (Figure 8D). Notably though, PyMT-RID^{MMTV} mice showed a significant reduction in tumor growth accompanied by an increase in body weight (Figure 8E-G), demonstrating an effect 410 opposite to that observed in PyMT-RID^{ad} mice. Lastly, CLS occurrence and TAM accumulation were comparable between PyMT-RID^{MMTV} and control mice (Figure 8H-J; Supplemental Figure 24; detailed images). To determine whether RID α/β alters tumor cell proliferation in a cell-autonomous manner or through interactions with the TME, we performed proliferation assays using an immortalized PyMT cell line. RID α/β overexpression dramatically reduced the 415 proliferation of these tumor cells (Supplemental Figure 25), suggesting that cell autonomous effects play a relevant role. Taken together, our observations indicate that the inhibition of inflammation directly in the tumor cells delays tumor growth but does not affect tumor onset or local macrophage accumulation. The manifestation of distinct phenotypes in the PyMT-RID^{MMTV} and PyMT-RID^{ad} models suggests that an inhibition of inflammatory signaling in tumor cells or 420 distinct cell types in the TME has complex effects on tumor development. This underscores the

critical need to better understand how inflammatory signaling in distinct cell types of shapes cancer development and progression.

Discussion

425 In this study, we investigated the intricate interplay of adipocyte inflammation, tumor cell
inflammation, macrophage dynamics, and mammary tumor development. Our approach involved
taking advantage of RID^{ad} mice and breeding them with the MMTV-PyMT mammary tumor model
to generate PyMT-RID^{ad} mice. This cross facilitated the examination of a targeted suppression of
inflammation in adipocytes and its specific impact on mammary tumor progression. Furthermore,
430 we extended our studies by breeding RID^{MMTV} mice with the MMTV-PyMT mammary tumor model
to generate PyMT-RID^{MMTV} mice. This approach enabled a comparative analysis of the impact of
cell-specific inflammation suppression on mammary cancer development and progression.
Through these distinct mouse models, our findings unveiled unique relationships, particularly the
crucial role of the adipocyte, in determining the tumor microenvironment.

435

Long-term HFD challenge of RID^{ad} mice

Our studies using RID^{ad} mouse model revealed a complex interplay between adipocyte
inflammation, adipocyte apoptosis, and macrophage dynamics (Figure 2 and Figure 3). The
observed upregulation of macrophage-related markers in the MFP and gWAT suggests a
440 potential link between dysregulated adipocyte inflammatory signaling and immune cell infiltration.
Supporting this notion, we observed concurrent phenomena of increased adipocyte apoptosis
and formation of CLSs following selective suppression of adipocyte inflammation (Figure 2).
Moreover, the phenomenon of macrophage accumulation in the MFP of RID^{ad} mice was similar
to that of TAMs (Figure 3), suggesting that suppression of adipocyte inflammation may create a
445 tumor-favorable microenvironment, thereby promoting tumor growth (43-46). The significant
upregulation of *Ccl2* in both the MFP and gWAT of RID^{ad} mice, along with the increased presence
of macrophages that resemble TAMs, highlights the importance of *Ccl2* in driving macrophage
infiltration and polarization. The observed upregulation of M2 macrophage-related genes further
supports the notion of *Ccl2* promoting local macrophage polarization (47, 48), indicating a

450 potential feedback loop between adipose tissue inflammation and immune modulation in female mice. These results highlight the multifunctional role of *Ccl2* in adipose tissue inflammation and provide insights into its impact on the TME. To address the observed discrepancy in the regulation of inflammatory genes between male and female mice, we investigated the cellular source of inflammatory gene induction in the MFP of RID^{ad} mice. Our findings suggest that this induction is
455 driven by cell types other than adipocytes. While isolated adipocytes from the MFPs of RID^{ad} mice did not exhibit increased inflammatory gene expression, the upregulation of *Ccl2* and M2 macrophage markers in whole MFPs indicates that infiltrating immune cells are the crucial contributors to the observed inflammatory environment.

460 **Long-term HFD challenge of PyMT-RID^{ad} mice**

Transitioning to the PyMT-RID^{ad} mouse model, our focus shifted to the MFP, considering its crucial role in breast cancer development. Strikingly, we observed that the suppression of adipocyte inflammatory signaling led to abnormal mammary gland development and significantly accelerated mammary tumor onset and growth (Figure 4). This coincided with elevated levels of
465 Ki67-positive cells and increased blood vessel formation. Importantly, metabolic dysfunction was observed in the surrounding adipose tissue, characterized by a decrease in the uptake of fatty acids, while tumors exhibited increased expression of CD36 and enhanced fatty acid uptake, suggesting a metabolic shift towards fatty acid utilization in the tumor itself, at the expense of the surrounding adipocytes (Figure 5). This metabolic shift indicated a potential redirection of lipid
470 resources to fuel the highly proliferative tumor growth in PyMT-RID^{ad} mice.

Short-term HFD challenge of PyMT-RID^{ad} mice

To gain an understanding of the processes that foster early tumor development, we also explored the changes occurring in the MFP of PyMT-RID^{ad} mice at an early stage. Notably, a
475 short-term HFD challenge of PyMT-RID^{ad} mice induced increased CLSs formation, indicative of

heightened adipocyte apoptosis, and macrophage recruitment (Figure 6). However, we did not detect elevated levels of cleaved caspase-3 at this stage, which may result from the still efficient and rapid clearance of dying cells by local macrophages. Full activation of caspase-3, may require prolonged signaling, becoming more evident at 12 weeks. Additionally, while *Ccl2* was significantly upregulated in the MFP of RID^{ad} mice after 12 weeks of Dox-HFD (Figure 1), it was not significantly changed in the MFP of PyMT-RID^{ad} mice after 4 weeks of Dox-HFD (Supplemental Figure 19). This phenomenon likely reflects a process in which macrophages initially aggregate around apoptotic or dysfunctional adipocytes induced by RID α/β , gradually transitioning toward a more TAM-like phenotype and subsequently expressing *Ccl2*. This suggests that the observed differences in *Ccl2* expression between RID^{ad} and PyMT-RID^{ad} mice may be driven by the gradual accumulation and activation of macrophages over time. Importantly, despite the slight reduction in *Ccl2* expression, PyMT-RID^{ad} mice still demonstrated the recruitment and accumulation of TAMs (Figure 6), indicating that TAM recruitment emerges as a critical factor influencing early tumor growth. In our RNA-seq analysis of the inguinal MFP of PyMT-RID^{ad} mice after the 4 weeks of Dox-HFD, we discovered compelling relationships between suppressed inflammation, altered insulin signaling, and rewired cellular metabolism. Specifically, we observed a downregulation of glycolysis- and glycogen metabolism-related gene expression (Supplemental Figure 19). These alterations coincide with lowered systemic insulin sensitivity in these mice. Pathway analyses support impaired insulin signaling in the MFP of PyMT-RID^{ad} mice, including a downregulation of the PI3K-Akt pathway (Supplemental Figure 20). Moreover, thermogenic processes within adipose tissue, including the browning of white adipocytes, relies on proper insulin signaling (49). Illustrating this dependence, E4orf1 overexpression mice display not only diminished insulin signaling but also reduced adipocyte browning (50). This suggests that disrupted insulin signaling in the MFP of PyMT-RID^{ad} mice may be a crucial driver of the observed downregulation of glycolysis, glycogen, and browning/beiging-related genes. Particularly, it has been shown that reduced glycolysis is linked to decreased thermogenesis, potentially

exacerbating insulin resistance (49, 51). Importantly, decreased uptake of lipids by adipose tissue due to insulin resistance may also enable tumors to take up and metabolize more lipids. This may effectively enhance tumor growth and metastasis through the upregulation of tumor progression- and metastasis-related genes as well as genes related to mammary gland and duct morphogenesis. Interestingly, our findings also indicate that RID α/β overexpression in adipocytes promotes an immunosuppressive tumor microenvironment through upregulation of *Ido1*, *Mrc1*, and *Cd200*. Despite no relevant changes in major immune cell populations such as M1 macrophages, dendritic cells, NK cells, or T cells, the elevated expression of these immunoregulatory genes, particularly IDO1, suggests that RID α/β -driven immune modulation may facilitate tumor immune escape in conjunction with TAM-mediated immune modulation.

Long-term HFD challenge of in PyMT-RID^{MMTV} mice

Intriguingly, the suppression of tumor cell inflammation in the PyMT-RID^{MMTV} model resulted in outcomes distinct from those in the PyMT-RID^{ad} model (Figure 8). Abnormal mammary gland development was minimal, emphasizing the tumor-specific effects of inflammation inhibition. Although tumor onset remained comparable between the groups, a significant reduction in tumor growth was observed in PyMT-RID^{MMTV} mice without affecting the number of CLSs (Figure 8). The recruitment of TAMs slightly decreased, which is consistent with a reduction in tumor growth, suggesting that the accumulation of TAMs near the tumor is a critical driver of tumor progression (Figure 8). The observed reduction in abnormal mammary gland development and tumor growth highlights the potential therapeutic significance of targeting inflammation in a tumor cell-selective manner. Further investigations into the underlying mechanisms governing the recruitment of TAMs and their impact on tumor progression appears necessary. Notably, the divergent phenotypes of the PyMT-RID^{ad} and PyMT-RID^{MMTV} models underscore the cell-specific effects of the inhibition of inflammation on mammary tumor development.

Collectively, our studies using distinct mouse models provide comprehensive insight into the cell type-specific contributions of inflammation to mammary tumor development and progression. The varying outcomes observed in different models emphasize the need for a careful assessment regarding targeting inflammation for therapeutic purposes, be it in adipocytes or in tumor cells. They may, ultimately, also have an impact on the effectiveness of checkpoint inhibitors, which can trigger inflammation and thereby hinder their effectiveness.

Methods

535 ***Sex as a biological variable***

This study exclusively examined female mice because the disease modeled, breast cancer, predominantly affects females.

Mouse models

All animal experimental protocols, including those for mouse use and euthanasia, were reviewed and approved by the Institutional Animal Care and Use Committee (IACUC) of the University of Texas Southwestern (UTSW) Medical Center under the animal protocol number 2015-101207. The transgenic strains, adipocyte-specific, doxycycline-inducible RID α/β -transgenic mice (*Adipoq-rtTA* \times *TRE-RID α/β* mice or RID^{ad}), were generated by our laboratory as previously described (1, 7). We established spontaneous breast tumor development mouse models by introducing these transgenes into the *MMTV-PyMT* mammary tumor model (PyMT-RID^{ad}). To establish mammary gland epithelial cell-specific, doxycycline-inducible RID α/β -transgenic mice with *MMTV-PyMT* (PyMT-RID^{MMTV}), RID^{ad} mice were crossed with *MMTV-rtTA/MMTV-PyMT* mice. *Adipoq-rtTA* was washed out and replaced with *MMTV-rtTA*. The transgenic strains *MMTV-rtTA* and *MMTV-PyMT* mice were previously generated and characterized by our laboratory (52). In each experiment, littermate mice that lacked the *TRE-RID α/β* transgene were chosen as control. These control mice were fed the same diet as the experimental group carrying the *TRE-RID α/β* transgene, *i.e.* either HFD or Dox-HFD. All mice used in this study, including littermate controls, were maintained on a pure C57BL/6 genetic background. Mice were housed under barrier conditions on a 12-hour light/dark cycle in a temperature-controlled environment (22°C) with *ad libitum* access to autoclaved water and diet. Cages were changed every other week, and constant veterinary supervision was provided. Diets used in this study include regular chow diet (LabDiet #5058), high-fat diet (HFD, 60% calorie from fat, Bio-Serv #S1850), and doxycycline HFD (Dox-HFD, 600 mg/kg, 60% calorie from fat, Bio-

Serv #S5867). Only female mice were used, as females are susceptible to the development of
560 mammary tumors.

Genotyping PCR

The small portion of the mouse tail tip was lysed in 100 μ l of 50 mM NaOH at 95°C for 1.5
hours and then neutralized by adding 10 μ l of 1M Tris-HCl (pH 8.0). After vortexing and a brief
spin down, 1 μ l of the supernatant was utilized as the PCR template. The primer pairs for
565 genotyping PCR are listed in Supplemental Table 2. The PCR program consisted of an initial step
at 95°C for 1 minute, followed by 30-35 cycles of 95°C for 15 seconds, 60°C for 30 seconds, and
72°C for 30 seconds, concluding with a final step at 72°C for 3 minutes. The size of the amplified
DNA was confirmed using 1-2% agarose gel electrophoresis with ethidium bromide (EtBr) staining.

EO771 syngeneic breast cancer model

570 To establish the EO771 syngeneic breast cancer model, EO771 cells (10^5 cells in 50 μ l,
mixed in a 1:1 ratio with PBS and Matrigel) were injected subcutaneously into the mammary fat
pad of 16-weeks-old mice that had been fed a HFD for 8 weeks. One week after cell injection,
mice with subcutaneous tumors reaching approximately 100 mm³ were selected for each group
and switched to a doxycycline-containing HFD. Tumor growth was monitored and measured using
575 electronic calipers approximately every two days. Tumor volume was calculated using the
modified ellipsoid formula: Tumor volume = $\frac{1}{2}$ (length \times width²). Animals were euthanized 21 days
post-injection.

Metabolic phenotyping

Assessments of systemic metabolism, including the oral glucose tolerance tests (OGTTs),
580 insulin tolerance tests (ITTs), and triglyceride tolerance tests (TGTTs), were performed as
previously described (53). **For OGTTs**, mice were fasted for 4-6 hours and subjected to an oral
gavage of dextrose (2.5 mg/g body weight). Tail blood was collected at 0, 15, 30, 60, and 120 min
in capillary tubes and prepared for serum and assayed for glucose. **For ITTs**, random-fed mice
were administered insulin (1.5 U/kg Humulin R; Eli Lilly) by intraperitoneal injection. Serum

585 glucose level was measured at 0, 15, 30, 60, and 120 minutes. ***For TGTTs***, mice were fasted for 16 hours and subjected to an oral gavage of 20% Intralipid (10 µl/g BDW, I141-100mL, Sigma). Tail blood was collected was collected at 0, 1.5, 3, and 6 hours for triglyceride, NEFA, and glycerol assays. Glucose, insulin, and triglyceride levels were measured using Contour blood glucose monitor (9545C; Bayer), oxidase-peroxidase assay (Sigma), insulin ELISA (Crystal Chem), and
590 Infinity Triglycerides Reagent (Thermo Fisher Scientific), respectively. NEFA were measured by free fatty acid quantification kits (Wako Diagnostics-NEFA-HR2).

Triolein uptake assay

Triolein uptake was measured as described previously (54). Briefly, mice were fasted for 16 hours and ³H-triolein (PerkinElmer, #NET431001MC; 2 µCi per mouse in 100 µl of 5%
595 intralipid) was administered by retro-orbital injection. Blood samples of 150 µl were collected at 1, 2, 5, 10, and 15 minutes. At the 15-minute mark, mice were euthanized, additional blood samples were obtained, and select tissues were promptly excised, weighed, flash-frozen in liquid nitrogen, and stored at -80°C until further processing. Tissue radioactivity, including blood samples, was quantified using a Tri-Carb 2910 TR scintillation counter (PerkinElmer).

Tissue preparation and immunostaining

Mice were euthanized by cervical dislocation following isoflurane anesthesia. Subsequently, tissues were promptly collected and fixed in 10% buffered formalin (Fisher) for 24 hours at room temperature. Afterwards, the tissues were rinsed with 50% ethanol, followed by embedding in paraffin blocks and cutting into 5 µm sections. ***For immunofluorescence staining***,
605 5 µm paraffin sections were baked for 30 minutes at 60°C and deparaffinized in xylene and ethanol, followed by boiling in Antigen Retrieval Solution (Vector Labs) containing 0.1% Tween-20. Slides were blocked in blocking buffer consisting of 10% goat serum (ThermoFisher) in PBS-T (0.1% Tween-20 in PBS) for 1 hour at room temperature and then overnight at 4°C with the primary antibodies RIDβ, Perilipin (Fitzgerald), cleaved caspase-3 (Cell Signaling), MAC-2
610 (BioLegend), CD163 (ProteinTech), Ki67 (Abcam), CD31 (Invitrogen), CD36 (Invitrogen), FABP4

(Invitrogen), and ER α (Home-made). The next day, slides were washed five times with PBS-T and incubated with secondary antibodies labeled with Alexa Fluor 488 (Thermo-Fisher) or Alexa Fluor 594 (Thermo-Fisher) diluted in blocking buffer for 1 hour at room temperature. Slides were washed five times with PBS-T, and then they were mounted with VECTASHIELD mounting
615 medium with DAPI (Vector Labs). Immunofluorescence staining was imaged using a Zeiss LSM880 confocal microscope (Zeiss) and analyzed by FIJI/ImageJ (VERSION: 2.1.0/1.53h). Image quantification was performed by merging the channel of the protein of interest with DAPI. Cells positive for the protein of interest were then counted and expressed as a percentage of the total nuclei. For CD31, the positive area was measured as a percentage of the total area in the
620 field. All image quantifications were performed using 2-3 mice per group. H&E staining was performed using standard reagents (Abcam). All details for antibodies and reagents are listed in Supplemental Table 3.

Tumor dissociation and primary tumor cell preparation

Approximately 0.5 mg of tumor tissue was excised from euthanized mice and finely minced on a
625 sterile surface. The minced tissue was incubated in a digestion buffer containing collagenase B, collagenase D, and DNase I at 37 °C with gentle stirring for 15–30 minutes. Following enzymatic digestion, the cell suspension was filtered through a 70 μ m cell strainer, centrifuged, washed, and treated with red blood cell lysis buffer. Cells were then resuspended in DMEM supplemented with 10% FBS and 10% horse serum, and subsequently subculture. Differential trypsinization was
630 used to separate tumor cells from non-tumorigenic cells during passaging.

Adipocytes size measurement

For adipocyte size quantification, brightfield H&E-stained images were acquired using a NanoZoomer S60 (Hamamatsu). Adipocyte size analysis was performed according to previously validated protocols with minor modifications (55). FIJI/ImageJ software was used to analyze and
635 calculate the area of each adipocyte. At least 200 adipocytes were quantified for each individual mouse.

Isolation of floated adipocytes, stromal vascular fraction cells, and generation of in vitro-differentiated adipocytes

The mammary fat pad of 4-6-weeks-old female mice was minced and digested for 1 hour at 37°C in a shaking water bath in Hank's Balanced Salt Solution (Sigma-Aldrich) containing 1.5% BSA (Sigma-Aldrich) and 1 mg/mL collagenase D (Roche). Samples were mixed every 20 minutes by gently inverting the tube to ensure uniform tissue digestion. The resulting dispersed tissue was filtered through a 100 µm cell strainer and centrifuged for 5 min at 600 g, 4°C. Floating adipocytes were collected, and the pelleted stromal vascular fraction (SVF) cells were resuspended in culture media (DMEM/F12 containing 10% FBS, 1x GlutaMax, 1x penicillin/streptomycin, and 1x gentamicin), filtered through a 45 µm cell strainer, and underwent a second round of centrifugation. The pelleted cells were resuspended in culture media and grown at 37°C in 5% CO₂. **For in vitro differentiation experiments**, SVF cells were grown to ~95% confluency and adipogenesis was induced using culture media supplemented with 500 µmol/l 3-isobutyl-1-methylxanthine, 1 µmol/l dexamethasone, 5 µg/ml insulin, and 1 µmol/l rosiglitazone for 2 days. Following induction, the cells were maintained in media containing only 5 µg/ml insulin and were used for harvesting the conditioned medium at 6-8 days of differentiation.

Preparation of conditioned medium (CM)

Serum-free CM was collected from *in vitro*-differentiated adipocytes from each group of mice. The collected CM was centrifuged at 2,000 rpm at 4°C for 10 minutes to remove any cellular debris. The supernatant was saved, aliquoted, flash-frozen in liquid nitrogen, and stored at -80°C.

Cancer cell culture

Human breast cancer cell lines including MCF-7, MDA-MB-231, HCC-1954, and HCC38, were sourced from the ATCC. Mouse breast cancer cell lines, including Met1 and EO771, were generously provided by the Brekken Lab at the University of Texas Southwestern Medical Center. All cells were maintained in RPMI (Gibco) supplemented with 10% fetal bovine serum (GeminiBio)

and 1% penicillin/streptomycin (Sigma-Aldrich). All details for cell lines and reagents are listed in Supplemental Table 3.

Cell proliferation assays

665 Cell proliferation assays were performed as described previously (56, 57). Briefly, human and mouse breast cancer cells were plated and grown in CM (conditioned media, see below) harvested from *in vitro*-differentiated adipocytes from each group of mice. The CM was replenished every other day for the specified durations before assessing cell proliferation. Cell proliferation was assessed every 2 days through a crystal violet staining assay. To this end, the
670 cells were washed with PBS, fixed with 5% formaldehyde for 10 minutes at room temperature, and stored in PBS at 4°C until all time points had been collected. The fixed cells were stained with a 0.1% crystal violet in a 20% methanol solution. After washing to remove unincorporated stain, the crystal violet was extracted using 10% glacial acetic acid and the absorbance was read at 595 nm.

Protein extraction and Western Blotting

675 Frozen tissues were crushed into a fine powder using a Tissue Pulverizer, ensuring that the tissues remained frozen during the process. The frozen powder was transferred to a glass douncer, then resuspend it in RIPA Buffer (10 mM Tris-HCl, pH 8.0; 1 mM EDTA; 0.5 mM EGTA; 1% Triton X-100; 0.1% Sodium Deoxycholate; 0.1% SDS; 140 mM NaCl) (Pierce) was added,
680 and the tissue was disrupted by douncing 10-20 times on ice. The mixture was transferred into a tube and incubated it with gentle mixing for 15 minutes at 4°C. The mixture was subjected to centrifugation at maximum speed multiple times in a microcentrifuge for 10 minutes at 4°C to remove the insoluble material and the supernatant was collected. Protein concentrations were determined using a BCA Protein Assay (Pierce). ***For Western blotting***, 20 µg of protein were
685 separated on a 4-12% gradient polyacrylamide-SDS gel (Invitrogen) and transferred onto a nitrocellulose membrane (BioRad). The membranes were blocked for 1 hour at room temperature in Tris-Buffered Saline (TBS) with 0.1% Tween (TBS-T) containing 5% non-fat dry milk. Primary

antibodies RID β (rabbit polyclonal; Home-made), cleaved caspase-3 (Cell Signaling), GAPDH (Invitrogen), and b-Actin (Cell Signaling) were diluted in 5% non-fat dry milk (Fisher scientific) and
690 incubated with membranes overnight at 4°C with gentle mixing. After extensive washing with TBS-T, the membranes were incubated with an appropriate HRP-conjugated secondary antibody (ThermoFisher) diluted in 1% non-fat dry milk for 1 hour at room temperature. The membranes were washed extensively with TBS-T before chemiluminescent detection using SuperSignal West Pico substrate (ThermoFisher) and an iBright 1500 system (Invitrogen). All details for antibodies
695 and reagents are listed in Supplemental Table 3.

RNA extraction and quantitative PCR (qPCR)

Total RNA was extracted from tissues using the RNeasy Mini kit (Qiagen), Trizol (Invitrogen), and EZ-10 DNAaway RNA miniprep kit (BIO BASIC) and cDNA pools were generated by reverse transcription using PrimeScript RT Master Mix (TaKaRa). Quantitative real-
700 time PCR (qPCR) was performed using Powerup SYBR Green PCR Master Mix (Applied Biosystems) on a Quantistudio 6 Flex Real-Time PCR System (Applied Biosystems). Primer sequences for qPCR are listed in Supplemental Table 1.

RNA-seq and bioinformatic analysis

RNA sequencing was performed by Novogene (Sacramento, CA, USA) as described
705 previously (53). Briefly, RNA isolated from the mammary fat pad or tumors was used to prepare an RNA-seq library by enrichment from total RNA using oligo(dT) beads. ***Bioinformatic analysis*** Novogene provided basic RNA-seq analysis, including the list of differentially regulated genes, pathway analysis and a heatmap. Differential gene expression analysis employed DESeq2, applying criteria of adjusted p-value (p_{adj}) ≤ 0.05 and absolute log₂ fold change
710 ($|\log_2\text{FoldChange}| \geq 1.0$) to identify significantly differentially expressed gene. The volcano plot was generated using Prism (GraphPad; Version 10.4.2) with genes from the entire gene list, including differentially regulated genes between two samples. Individual gene data expressed as mean \pm SEM were obtained using FPKM or log₂(FPKM) from RNAseq. Gene Set Enrichment

715 Analysis (GSEA) was performed using the GSEA module available in Gene Pattern (version 20.4.0; Broad Institute; <https://www.genepattern.org/>). The Hallmark gene sets from the Molecular Signatures Database (MsigDB v2024.1, Broad Institute) were used to identify enriched pathways. GSEA was conducted with default settings, with minor modifications, including weighted scoring, phenotype-based permutations (1,000 permutations), gene ranking using the t-test, and standard normalization methods.

720 **Statistics**

All data were expressed as mean \pm SEM. Differences between two groups were examined for statistical significance by the unpaired 2-tailed Student's *t*-test. 2-way Analysis of variance test (ANOVA) with a multiple comparison test using Prism software (GraphPad, San Diego, Calif., USA) was applied to multiple time point comparisons. *P*-values and adjusted *P*-values for RNA-725 seq were determined by use of DESeq2 R package. *P* value <0.05 denoted the presence of a statistically significant difference. Each respective statistics methodology used is described in the respective Figure Legend.

Study approval

All animal procedures were approved by the IACUC of The University of Texas Southwestern 730 Medical Center (APN no. 2015-101207).

Data availability

All data supporting the findings of this study are available within the article and its supplementary materials, including Source Data. RNA sequencing data are available at NCBI GEO under the accession code (GSE276790). Values for all data points in graphs are reported in the [Supporting 735 Data Values](#) file.

Author contributions

P.E.S. conceived the project. D-S.K. and P.E.S. designed the experiments and supervised their implementation. D-S.K. and T.O. performed most of mouse-based experiments together. D-S.K.

conducted all cell-based experiments. Q.Z. and M.K. provided RID^{ad} mice and intellectual input
740 for this manuscript. X.S. conducted triolein uptake assay with assistance from D-S.K. and T.O. J-
B.F, K.M., M.K., C.J., and C.L. provided assistance in interpreting the results and with mouse-
related tasks. Q.L. and K.M. performed adipocyte measurement experiments. C.L., J.V., and M.P.
assisted with histology. D-S.K. prepared the initial drafts of the figures and text with the help of
T.O., which were then reviewed and edited by J-B.F., R.M.W., and P.E.S. The manuscript was
745 finalized by P.E.S. P.E.S. is the guarantor of this work and had full access to all the data in the
study, taking responsibility for its integrity and the accuracy of the analysis. P.E.S. secured
funding for the project and provided intellectual support across all aspects of the work. D-S.K. and
T.O. contributed equally to the conducted experiments and are recognized as co-first authors.
The order of the co-first authors was based on the role of D-S.K. was listed first because he
750 initiated the project, designed the experiments, and drafted the original manuscript.

Acknowledgments

We thank the following UT Southwestern Core facilities: UTSW Animal Resource Center
and Live Cell Imaging Core for microscopy. We also thank the members of the Scherer lab for
755 valuable insight and feedback on this manuscript. This work was supported by NIH grants R01-
DK55758, R01-DK099110, R01-DK127274, R01-DK131537 to P.E.S. and P01-AG051459 (Dixit),
as well as an AHA Career Development Award 855170 to Q.Z. NIH shared instrumentation grant
1S10OD021684-0 to Katherine Luby-Phelps. PES was also supported by NIDDK-NORC P30-
DK127984.

760

References

1. Wernstedt Asterholm I, Tao C, Morley TS, Wang QA, Delgado-Lopez F, Wang ZV, et al. Adipocyte inflammation is essential for healthy adipose tissue expansion and remodeling. *Cell Metab.* 2014;20(1):103-18.
- 765 2. Benedict CA, Norris PS, Prigozy TI, Bodmer JL, Mahr JA, Garnett CT, et al. Three adenovirus E3 proteins cooperate to evade apoptosis by tumor necrosis factor-related apoptosis-inducing ligand receptor-1 and -2. *J Biol Chem.* 2001;276(5):3270-8.
3. Delgado-Lopez F, and Horwitz MS. Adenovirus RIDalpha complex inhibits lipopolysaccharide signaling without altering TLR4 cell surface expression. *J Virol.* 770 2006;80(13):6378-86.
4. Lichtenstein DL, Krajcsi P, Esteban DJ, Tollefson AE, and Wold WS. Adenovirus RIDbeta subunit contains a tyrosine residue that is critical for RID-mediated receptor internalization and inhibition of Fas- and TRAIL-induced apoptosis. *J Virol.* 2002;76(22):11329-42.
- 775 5. Zanardi TA, Yei S, Lichtenstein DL, Tollefson AE, and Wold WS. Distinct domains in the adenovirus E3 RIDalpha protein are required for degradation of Fas and the epidermal growth factor receptor. *J Virol.* 2003;77(21):11685-96.
6. Lichtenstein DL, Toth K, Doronin K, Tollefson AE, and Wold WS. Functions and mechanisms of action of the adenovirus E3 proteins. *Int Rev Immunol.* 2004;23(1-2):75- 780 111.
7. Zhu Q, An YA, Kim M, Zhang Z, Zhao S, Zhu Y, et al. Suppressing adipocyte inflammation promotes insulin resistance in mice. *Mol Metab.* 2020;39:101010.
8. Greten FR, and Grivennikov SI. Inflammation and Cancer: Triggers, Mechanisms, and Consequences. *Immunity.* 2019;51(1):27-41.
- 785 9. Zhao H, Wu L, Yan G, Chen Y, Zhou M, Wu Y, et al. Inflammation and tumor progression: signaling pathways and targeted intervention. *Signal Transduct Target Ther.* 2021;6(1):263.
10. Danforth DN. The Role of Chronic Inflammation in the Development of Breast Cancer. *Cancers (Basel).* 2021;13(15).
- 790 11. Agnoli C, Grioni S, Pala V, Allione A, Matullo G, Gaetano CD, et al. Biomarkers of inflammation and breast cancer risk: a case-control study nested in the EPIC-Varese cohort. *Sci Rep.* 2017;7(1):12708.
12. Tobias DK, Akinkuolie AO, Chandler PD, Lawler PR, Manson JE, Buring JE, et al. Markers of Inflammation and Incident Breast Cancer Risk in the Women's Health Study. 795 *Am J Epidemiol.* 2018;187(4):705-16.
13. Pierce BL, Ballard-Barbash R, Bernstein L, Baumgartner RN, Neuhaus ML, Wener MH, et al. Elevated biomarkers of inflammation are associated with reduced survival among breast cancer patients. *J Clin Oncol.* 2009;27(21):3437-44.
14. Grivennikov SI, Greten FR, and Karin M. Immunity, inflammation, and cancer. *Cell.* 800 2010;140(6):883-99.
15. Colotta F, Allavena P, Sica A, Garlanda C, and Mantovani A. Cancer-related inflammation, the seventh hallmark of cancer: links to genetic instability. *Carcinogenesis.* 2009;30(7):1073-81.
16. Faria SS, Costantini S, de Lima VCC, de Andrade VP, Rialland M, Cedric R, et al. 805 NLRP3 inflammasome-mediated cytokine production and pyroptosis cell death in breast cancer. *J Biomed Sci.* 2021;28(1):26.
17. Manore SG, Doheny DL, Wong GL, and Lo HW. IL-6/JAK/STAT3 Signaling in Breast Cancer Metastasis: Biology and Treatment. *Front Oncol.* 2022;12:866014.

- 810 18. Attalla S, Taifour T, Bui T, and Muller W. Insights from transgenic mouse models of PyMT-induced breast cancer: recapitulating human breast cancer progression in vivo. *Oncogene*. 2021;40(3):475-91.
19. Lin EY, Jones JG, Li P, Zhu L, Whitney KD, Muller WJ, et al. Progression to malignancy in the polyoma middle T oncoprotein mouse breast cancer model provides a reliable model for human diseases. *Am J Pathol*. 2003;163(5):2113-26.
- 815 20. Yang H, Zhang Q, Xu M, Wang L, Chen X, Feng Y, et al. CCL2-CCR2 axis recruits tumor associated macrophages to induce immune evasion through PD-1 signaling in esophageal carcinogenesis. *Mol Cancer*. 2020;19(1):41.
21. Murano I, Barbatelli G, Parisani V, Latini C, Muzzonigro G, Castellucci M, et al. Dead adipocytes, detected as crown-like structures, are prevalent in visceral fat depots of genetically obese mice. *J Lipid Res*. 2008;49(7):1562-8.
- 820 22. Cinti S, Mitchell G, Barbatelli G, Murano I, Ceresi E, Faloia E, et al. Adipocyte death defines macrophage localization and function in adipose tissue of obese mice and humans. *J Lipid Res*. 2005;46(11):2347-55.
23. Maliniak ML, Miller-Kleinhenz J, Cronin-Fenton DP, Lash TL, Gogineni K, Janssen EAM, et al. Crown-Like Structures in Breast Adipose Tissue: Early Evidence and Current Issues in Breast Cancer. *Cancers (Basel)*. 2021;13(9).
- 825 24. Tan Y, Wang M, Zhang Y, Ge S, Zhong F, Xia G, et al. Tumor-Associated Macrophages: A Potential Target for Cancer Therapy. *Front Oncol*. 2021;11:693517.
25. Vitale I, Manic G, Coussens LM, Kroemer G, and Galluzzi L. Macrophages and Metabolism in the Tumor Microenvironment. *Cell Metab*. 2019;30(1):36-50.
- 830 26. Mantovani A, Allavena P, Marchesi F, and Garlanda C. Macrophages as tools and targets in cancer therapy. *Nat Rev Drug Discov*. 2022;21(11):799-820.
27. Ramos RN, Rodriguez C, Hubert M, Ardin M, Treilleux I, Ries CH, et al. CD163(+) tumor-associated macrophage accumulation in breast cancer patients reflects both local differentiation signals and systemic skewing of monocytes. *Clin Transl Immunology*. 2020;9(2):e1108.
- 835 28. Tiainen S, Tumelius R, Rilla K, Hamalainen K, Tammi M, Tammi R, et al. High numbers of macrophages, especially M2-like (CD163-positive), correlate with hyaluronan accumulation and poor outcome in breast cancer. *Histopathology*. 2015;66(6):873-83.
- 840 29. Zhang WJ, Wang XH, Gao ST, Chen C, Xu XY, Sun Q, et al. Tumor-associated macrophages correlate with phenomenon of epithelial-mesenchymal transition and contribute to poor prognosis in triple-negative breast cancer patients. *J Surg Res*. 2018;222:93-101.
30. Sousa S, Brion R, Lintunen M, Kronqvist P, Sandholm J, Monkkonen J, et al. Human breast cancer cells educate macrophages toward the M2 activation status. *Breast Cancer Res*. 2015;17(1):101.
- 845 31. Wang J, Mi S, Ding M, Li X, and Yuan S. Metabolism and polarization regulation of macrophages in the tumor microenvironment. *Cancer Lett*. 2022;543:215766.
32. Zhang X, Ji L, and Li MO. Control of tumor-associated macrophage responses by nutrient acquisition and metabolism. *Immunity*. 2023;56(1):14-31.
- 850 33. Wenes M, Shang M, Di Matteo M, Goveia J, Martin-Perez R, Serneels J, et al. Macrophage Metabolism Controls Tumor Blood Vessel Morphogenesis and Metastasis. *Cell Metab*. 2016;24(5):701-15.
34. Motoshima H, Goldstein BJ, Igata M, and Araki E. AMPK and cell proliferation--AMPK as a therapeutic target for atherosclerosis and cancer. *J Physiol*. 2006;574(Pt 1):63-71.
- 855 35. Liu J, Xiao Q, Xiao J, Niu C, Li Y, Zhang X, et al. Wnt/beta-catenin signalling: function, biological mechanisms, and therapeutic opportunities. *Signal Transduct Target Ther*. 2022;7(1):3.

- 860 36. Vayrynen JP, Haruki K, Lau MC, Vayrynen SA, Zhong R, Dias Costa A, et al. The Prognostic Role of Macrophage Polarization in the Colorectal Cancer Microenvironment. *Cancer Immunol Res.* 2021;9(1):8-19.
37. Nip C, Wang L, and Liu C. CD200/CD200R: Bidirectional Role in Cancer Progression and Immunotherapy. *Biomedicines.* 2023;11(12).
- 865 38. Meireson A, Devos M, and Brochez L. IDO Expression in Cancer: Different Compartment, Different Functionality? *Front Immunol.* 2020;11:531491.
39. Huang X, Zhang F, Wang X, and Liu K. The Role of Indoleamine 2, 3-Dioxygenase 1 in Regulating Tumor Microenvironment. *Cancers (Basel).* 2022;14(11).
40. Friberg M, Jennings R, Alsarraj M, Dessureault S, Cantor A, Extermann M, et al. Indoleamine 2,3-dioxygenase contributes to tumor cell evasion of T cell-mediated rejection. *Int J Cancer.* 2002;101(2):151-5.
- 870 41. Trinchieri G. Interleukin-12: a proinflammatory cytokine with immunoregulatory functions that bridge innate resistance and antigen-specific adaptive immunity. *Annu Rev Immunol.* 1995;13:251-76.
42. Verboven K, Wouters K, Gaens K, Hansen D, Bijnen M, Wetzels S, et al. Abdominal subcutaneous and visceral adipocyte size, lipolysis and inflammation relate to insulin resistance in male obese humans. *Sci Rep.* 2018;8(1):4677.
- 875 43. Bied M, Ho WW, Ginhoux F, and Bleriot C. Roles of macrophages in tumor development: a spatiotemporal perspective. *Cell Mol Immunol.* 2023;20(9):983-92.
44. Xiang X, Wang J, Lu D, and Xu X. Targeting tumor-associated macrophages to synergize tumor immunotherapy. *Signal Transduct Target Ther.* 2021;6(1):75.
- 880 45. Franklin RA, Liao W, Sarkar A, Kim MV, Bivona MR, Liu K, et al. The cellular and molecular origin of tumor-associated macrophages. *Science.* 2014;344(6186):921-5.
46. Qian BZ, and Pollard JW. Macrophage diversity enhances tumor progression and metastasis. *Cell.* 2010;141(1):39-51.
- 885 47. Sierra-Filardi E, Nieto C, Dominguez-Soto A, Barroso R, Sanchez-Mateos P, Puig-Kroger A, et al. CCL2 shapes macrophage polarization by GM-CSF and M-CSF: identification of CCL2/CCR2-dependent gene expression profile. *J Immunol.* 2014;192(8):3858-67.
48. Xu R, Li Y, Yan H, Zhang E, Huang X, Chen Q, et al. CCL2 promotes macrophages-associated chemoresistance via MCP1P1 dual catalytic activities in multiple myeloma. *Cell Death Dis.* 2019;10(10):781.
- 890 49. Czech MP. Mechanisms of insulin resistance related to white, beige, and brown adipocytes. *Mol Metab.* 2020;34:27-42.
50. Kusminski CM, Gallardo-Montejano VI, Wang ZV, Hegde V, Bickel PE, Dhurandhar NV, et al. E4orf1 induction in adipose tissue promotes insulin-independent signaling in the adipocyte. *Mol Metab.* 2015;4(10):653-64.
- 895 51. Winther S, Isidor MS, Basse AL, Skjoldborg N, Cheung A, Quistorff B, et al. Restricting glycolysis impairs brown adipocyte glucose and oxygen consumption. *Am J Physiol Endocrinol Metab.* 2018;314(3):E214-E23.
- 900 52. Zhu Q, Zhu Y, Hepler C, Zhang Q, Park J, Gliniak C, et al. Adipocyte mesenchymal transition contributes to mammary tumor progression. *Cell Rep.* 2022;40(11):111362.
53. Onodera T, Kim DS, Ye R, Wang MY, Chen S, Field BC, et al. Protective roles of adiponectin and molecular signatures of HNF4alpha and PPARalpha as downstream targets of adiponectin in pancreatic beta cells. *Mol Metab.* 2023;78:101821.
- 905 54. Onodera T, Wang MY, Rutkowski JM, Deja S, Chen S, Balzer MS, et al. Endogenous renal adiponectin drives gluconeogenesis through enhancing pyruvate and fatty acid utilization. *Nat Commun.* 2023;14(1):6531.

- 910 55. An YA, Crewe C, Asterholm IW, Sun K, Chen S, Zhang F, et al. Dysregulation of Amyloid Precursor Protein Impairs Adipose Tissue Mitochondrial Function and Promotes Obesity. *Nat Metab.* 2019;1(12):1243-57.
56. Kim DS, Camacho CV, Nagari A, Malladi VS, Challa S, and Kraus WL. Activation of PARP-1 by snoRNAs Controls Ribosome Biogenesis and Cell Growth via the RNA Helicase DDX21. *Mol Cell.* 2019;75(6):1270-85 e14.
- 915 57. Kim DS, Camacho CV, Setlem R, Kim K, Malladi S, Hou TY, et al. Functional Characterization of lncRNA152 as an Angiogenesis-Inhibiting Tumor Suppressor in Triple-Negative Breast Cancers. *Mol Cancer Res.* 2022;20(11):1623-35.

Figure legends

920 **Figure 1. RID α/β and inflammatory gene expression in RID^{ad} mice.**

(A) Schematic representation of adipocyte-specific, doxycycline-inducible RID α/β transgenic mice. (B and C) qPCR analysis of RID α/β mRNA expression in the mammary fat pad (MFP) (B) and gonadal white adipose tissue (gWAT) (C). *Rps16* and *36b4* were used for normalization. $n = 4-6$ /group. (D) Western blot analysis of RID β and GAPDH protein expression in different tissues from control (Ct) and RID^{ad} (R^a) mice. (E) Representative immunostaining of RID β and perilipin in the MFP. The magnified panels show adipocytes and mammary duct epithelial cells. (F) Representative immunostaining of RID β and perilipin in the MFP and gWAT. (G and H) qPCR analysis of inflammation-related mRNA expression in the MFP (G) and gWAT (H). *Rps16* and *36b4* were used for normalization. $n = 4-6$ /group. (Statistics) (B, C, G, H) Data are displayed as mean \pm SEM and were analyzed by unpaired 2-tailed t-tests. * $p < 0.05$, ** $p < 0.01$.
925
930

Figure 2. Increased adipocyte apoptosis and crown-like structure formation in RID^{ad} mice.

(A) Representative immunostaining of cleaved caspase-3 (C-CASP3) and perilipin in the mammary fat pad (MFP). (B) Quantification of the percentage of cleaved C-CASP3-positive cells from the experiments shown in (A). A total of 6 images from 3 control mice and 6 images from 3 RID^{ad} mice were quantified. (C) Representative immunostaining of C-CASP3 and perilipin in gonadal white adipose tissue (gWAT). (D) Quantification of the percentage of cleaved C-CASP3-positive cells from the experiments shown in (C). A total of 6 images from 3 control mice and 6 images from 3 RID^{ad} mice were quantified. (E) Representative immunostaining of MAC-2 and perilipin in the MFP. (F) Representative immunostaining MAC-2 and perilipin in gWAT. (G) Quantification of the number of CLSs, based on the experiments shown in (E and F), was performed on 4 control mice and 5 RID^{ad} mice. (Statistics) Data are displayed as mean \pm SEM and were analyzed by unpaired 2-tailed t-tests (B, D, G).
935
940

945 **Figure 3. Increased TAM accumulation and accelerated tumor growth in the MFP of RID^{ad} mice.**

(A) Representative immunostaining of CD163 and perilipin in the mammary fat pad (MFP). (B) Quantification of the percentage of CD163-positive cells from the experiments shown in (A). A total of 21-28 images from 3 mice per group were quantified. (C) Representative immunostaining
950 of CD163 and perilipin in gonadal white adipose tissue (gWAT). (D) Quantification of the percentage of CD163-positive cells from the experiments shown in (C). A total of 28-29 images from 3 mice per group were quantified. (E) Schematic representation of the experimental design for the EO771 syngeneic breast cancer mouse model. (F) Images of syngeneic tumors formed in each group. (G) Growth curves of transplanted EO771 cells. $n = 5/\text{group}$. (H and I) Tumor weight
955 (H) and body weight (I) at the end of the experiment. $n = 5/\text{group}$. (J and K) H&E staining of the MFP. (Statistics) Data are displayed as mean \pm SEM and were analyzed by unpaired 2-tailed t-tests (B, D, H, I) or two-way ANOVA (G). $**p = 0.01$, $****p < 0.0001$.

**Figure 4. Earlier mammary tumor onset, accelerated tumor growth, and a higher incidence
960 of lung metastasis in PyMT-RID^{ad} mice.**

(A) Schematic representation of the generation of PyMT-RID^{ad} mice by introducing RID^{ad} mice into the MMTV-PyMT mammary tumor model. (B) Analysis of the mammary fat pad (MFP) in PyMT-RID^{ad} mice revealed abnormalities in mammary gland development, as evidenced by H&E staining. Representative samples are shown. (C) Kaplan-Meier tumor-free mouse curves from 2
965 independent experiments. $n = 13-16/\text{group}$. (D and E) Tumor weight (D) and body weight (E) at the end of the experiment. $n = 13-16/\text{group}$. (F) Images of tumors formed in each group at the end of the experiments (mice approximately 20 weeks old). A circle indicates multiple tumors that were harvested from a single mouse. (G) Representative immunostaining of Ki67 in the tumors. $n = 3/\text{group}$. (H) Representative immunostaining of CD31 in the tumors. (I) Quantification of the
970 percentage of CD163-positive area from the experiments shown in (H). A total of 14-16 images

from 3 mice per group were quantified. **(J)** H&E staining shows metastatic breast tumor development in the lungs of PyMT-RID^{ad} mice. A magnified image of Ki67-immunostained tumor is provided. **(Statistics)** Data are displayed as mean±SEM and were analyzed by unpaired 2-tailed t-tests (D, E, I).

975

Figure 5. Metabolic dysfunction and increased lipid uptake in tumors of PyMT-RID^{ad} mice.

(A) Representative immunostaining of CD36 in the tumors. *n* = 3/group. The image of different area is shown in supplemental figure 7. **(B)** Representative immunostaining of FABP4 in the tumors. *n* = 3/group. **(C)** Schematic representation of the experimental design for the metabolic phenotyping, tumor development, and triolein uptake. *n* = 5-6/group. **(D)** Oral glucose tolerance test. **(E)** Intraperitoneal insulin tolerance test (ITT). **(F-I)** Triolein uptake into the tumor (F), mammary fat pad (MFP; G), gonadal white adipose tissue (gWAT; H), and liver (I). *n* = 5-6/group. **(Statistics)** Data are displayed as mean±SEM and were analyzed by unpaired 2-tailed t-tests (D-I).

985

Figure 6. Increased CLSs formation and TAMs accumulation at early stages of tumor development in PyMT-RID^{ad} mice.

(A) H&E staining of the mammary fat pad (MFP), encompassing both abdominal and inguinal pads. *n* = 3/group. **(B)** Representative immunostaining of Ki67 in the MFP. *n* = 3/group. Detailed images are shown in Supplemental figure 11. **(C)** Representative immunostaining of MAC-2 and perilipin in the MFP. **(D)** Quantification of the number of crown-like structures (CLSs) from the experiments shown in (C). *n* = 3/group. **(E)** Representative immunostaining of CD163 and perilipin in the MFP. Regions distant from and proximal to the tumor are shown. **(F)** Quantification of the number of tumor-associated macrophages (TAMs) from the experiments shown in (E). *n* = 3/group. **(Statistics)** Data are displayed as mean±SEM and were analyzed by unpaired 2-tailed t-tests (D and F).

995

Figure 7. Inflammation suppression in adipocytes alters the tumor microenvironment, metabolism, and immune landscape in PyMT-RID^{ad} mice.

1000 **(A)** Heatmap of differentially expressed genes by RNA-seq in the mammary fat pad (MFP). $n = 3$ /group. **(B)** RNA-seq analysis of tumor-associated macrophage (TAM) markers. **(C)** RNA-seq analysis of immunoregulatory molecules. **(D)** Representative immunostaining of IDO1 in the MFP, specifically in mammary gland and tumor regions. $n = 2-3$ /group. Detailed images are shown in supplemental figure 15. **(E)** RNA-seq of chemoattractant molecules. **(F)** Heatmap of differentially expressed apoptosis-related genes by RNA-seq in the MFP. **(Statistics)** Data are displayed as mean \pm SEM and were analyzed by unpaired 2-tailed t-tests (B, C, E). * $p < 0.05$, *** $p < 0.001$.

1005

Figure 8. Decelerated mammary tumor growth but unchanged tumor onset and tissue macrophage accumulation in PyMT-RID^{MMTV} mice.

1010 **(A)** Schematic representation of the generation of PyMT-RID^{MMTV} mice by introducing mammary gland epithelial cell-specific, doxycycline-inducible RID α/β transgenic mice into the MMTV-PyMT mammary tumor model. $n = 7-9$ /group **(B)** Representative immunostaining of RID β and perilipin in the mammary fat pad (MFP). **(C)** PyMT-RID^{MMTV} mice reveal reduced abnormalities in mammary gland development, as evidenced by H&E staining. **(D)** Kaplan-Meier tumor-free mouse curves from 2 independent experiments. $n = 7-9$ /group. **(E)** Tumor weight at the end of the experiment. $n = 6-8$ /group. **(F)** Images of tumors formed in each group at the end of the experiments (mice approximately 19-20 weeks old). In each group, 2 mice had to be sacrificed a week earlier due to a high tumor burden. $n = 6-8$ /group. **(G)** Body weight. $n = 7-9$ /group. Two-way ANOVA. * $p = 0.0$, ** $p < 0.01$. **(H)** Representative immunostaining of MAC-2 and perilipin in the MFP. **(I)** Quantification of the number of crown-like structures (CLSs) from the experiments shown in (H). $n = 4$ /group. **(J)** Representative immunostaining of CD163 and perilipin in the MFP. **(K)** Quantification of the number of tumor-associated macrophages (TAMs) from the experiments

1015

1020

shown in (J). $n = 4/\text{group}$. **(Statistics)** Data are displayed as $\text{mean} \pm \text{SEM}$ and were analyzed by unpaired 2-tailed t-tests (E, G, I, K).

1025

1030

1035

Figure 1 – Kim et al. (2025)

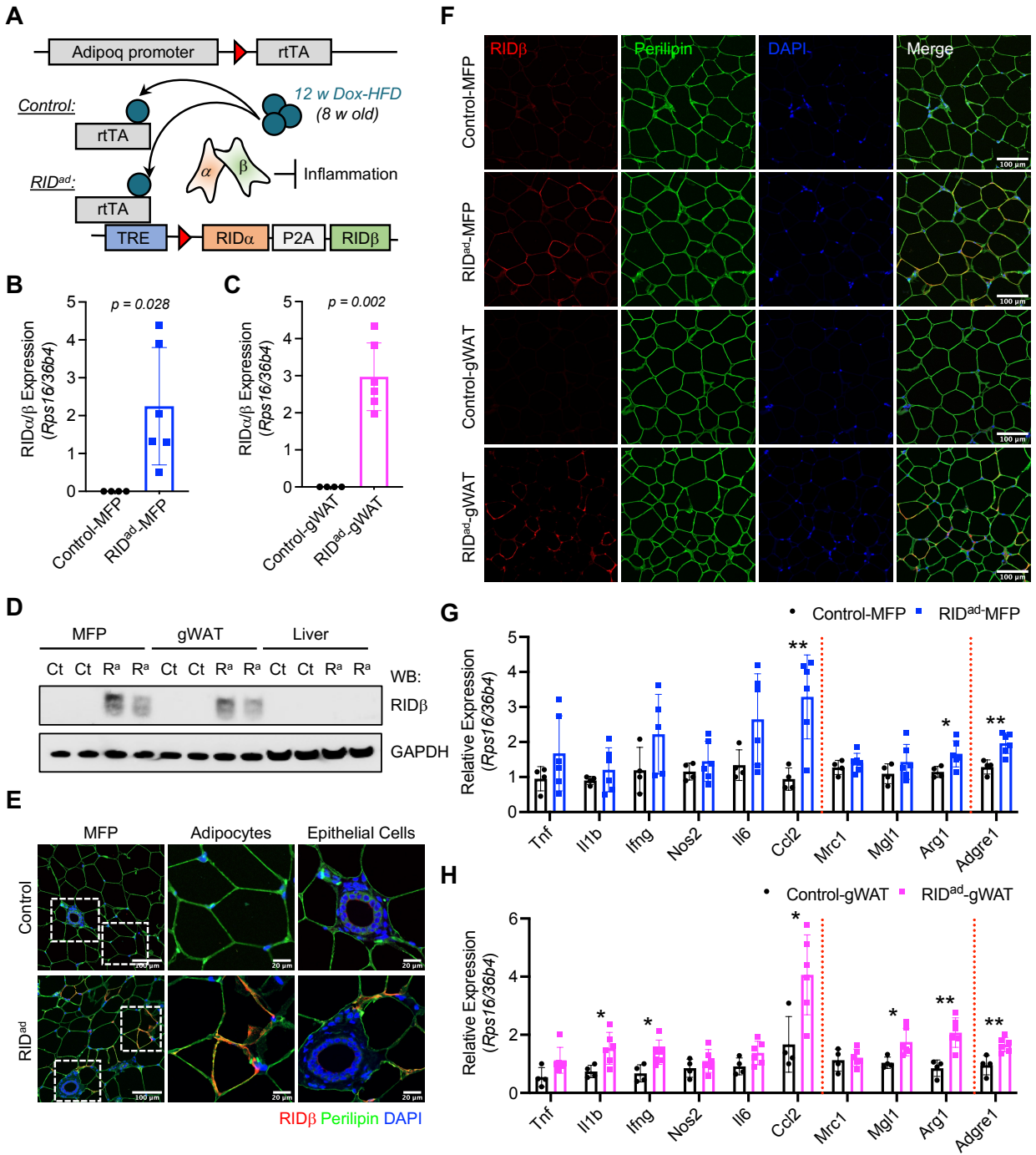
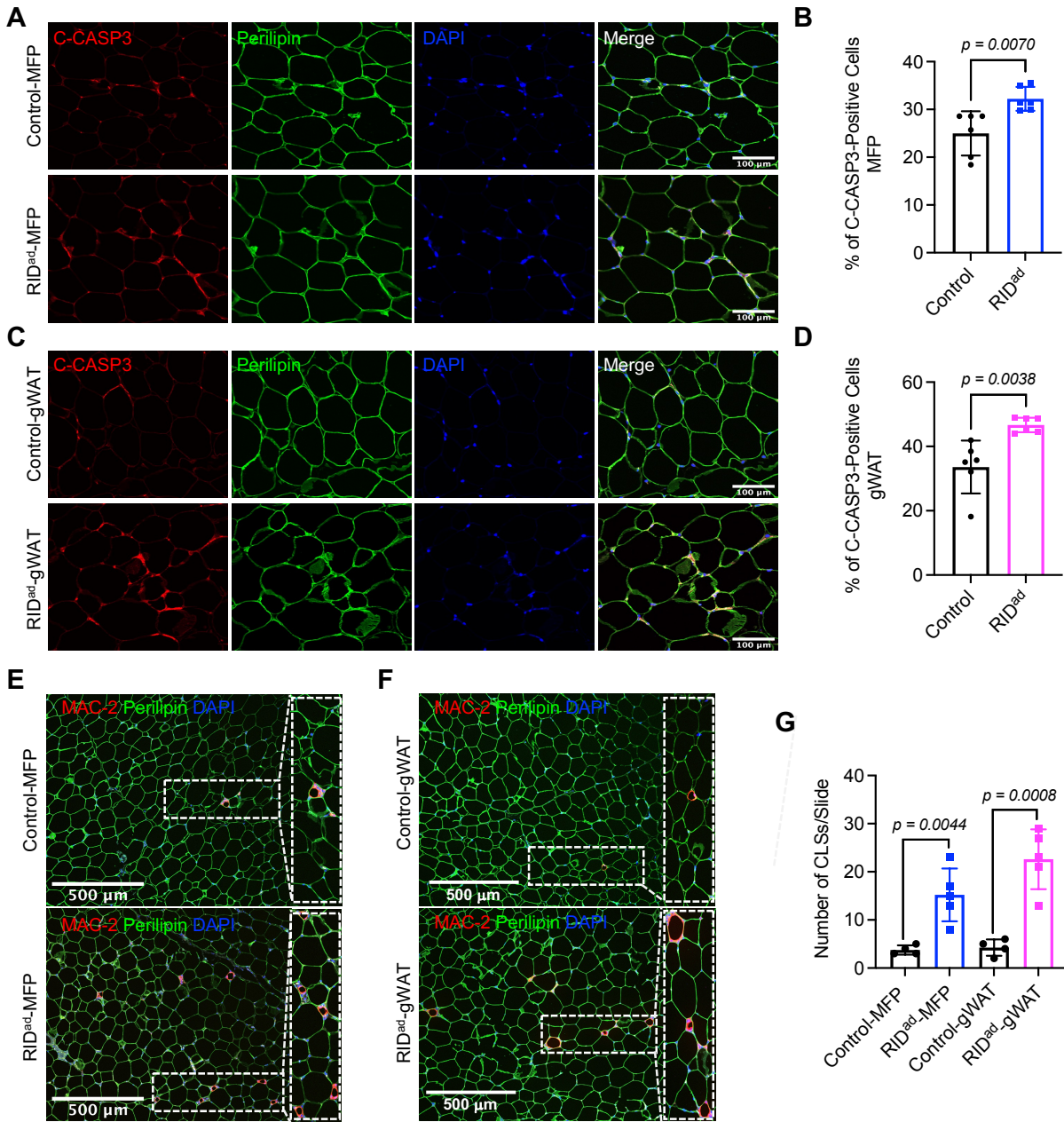


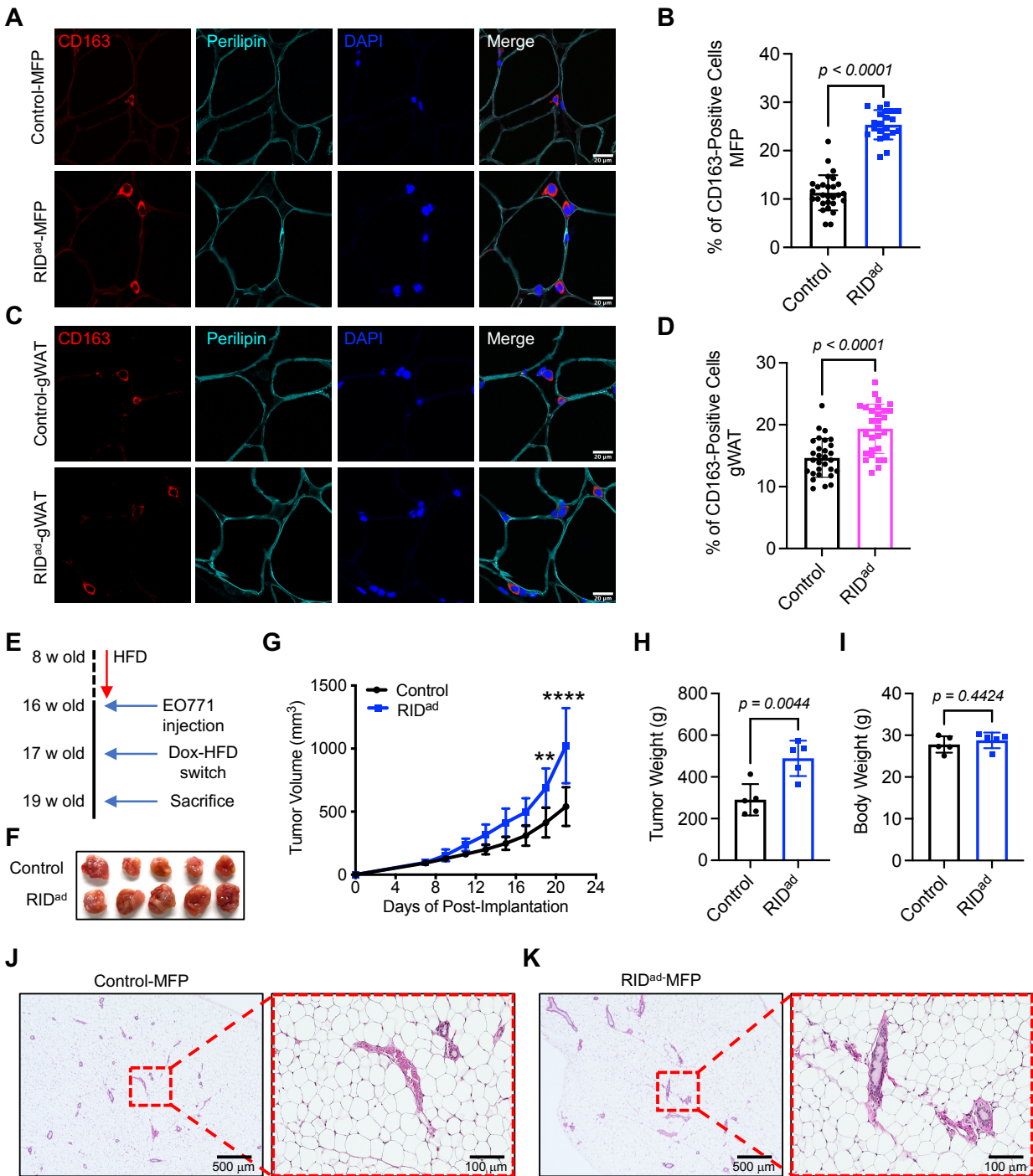
Figure 2 – Kim et al. (2025)



1045

1050

Figure 3 – Kim et al. (2025)



1055

1060

Figure 4 – Kim et al. (2025)

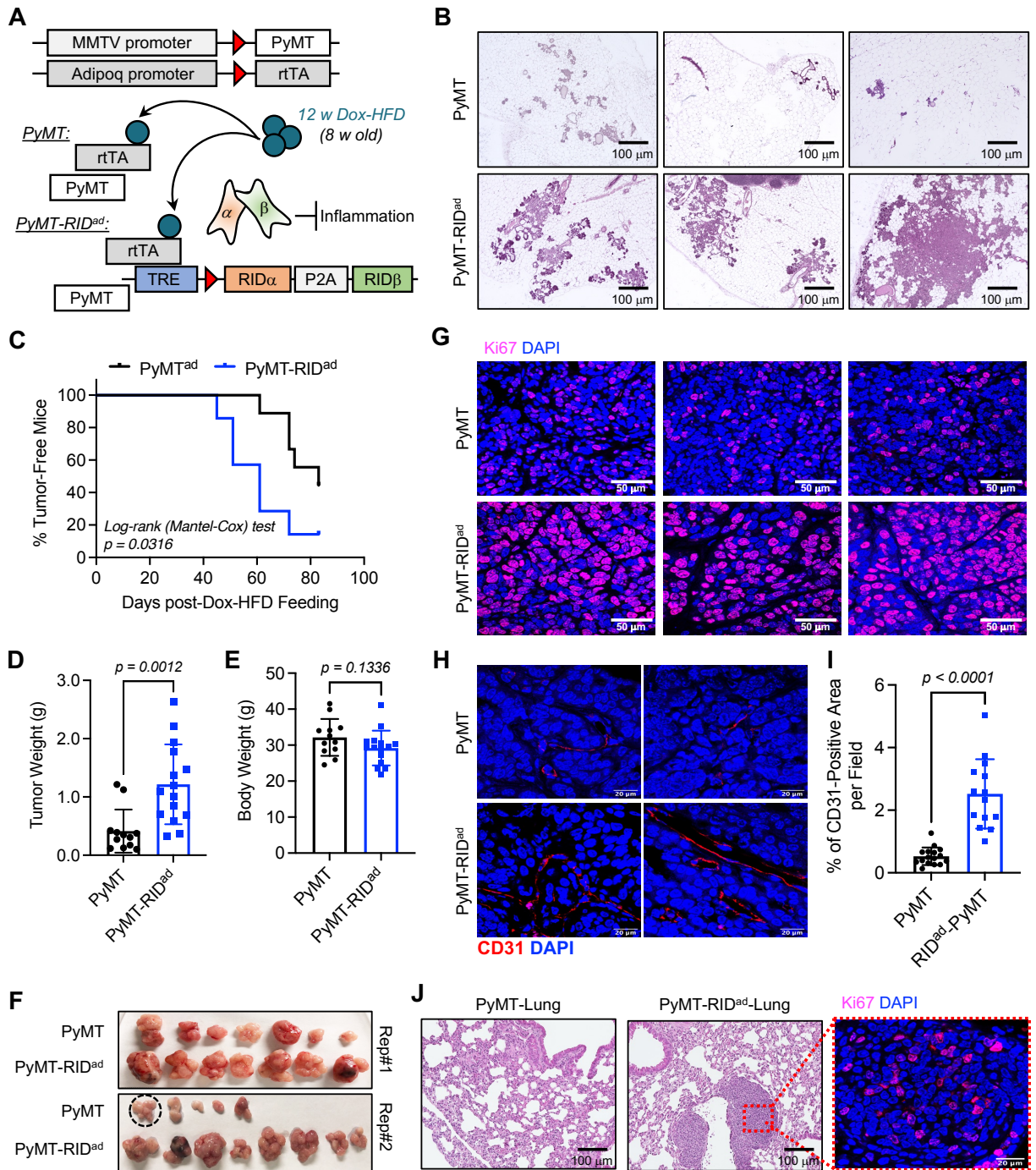
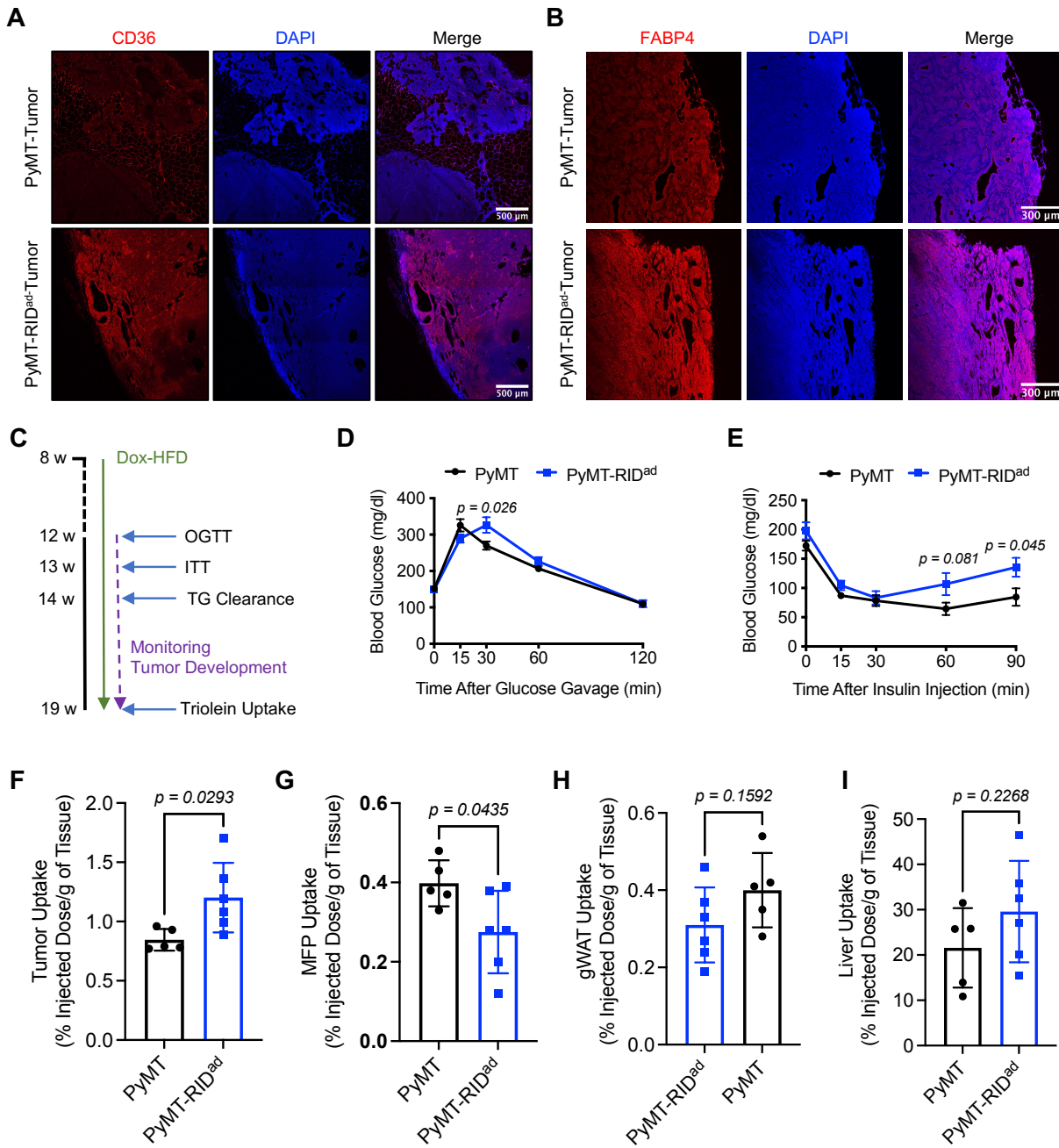


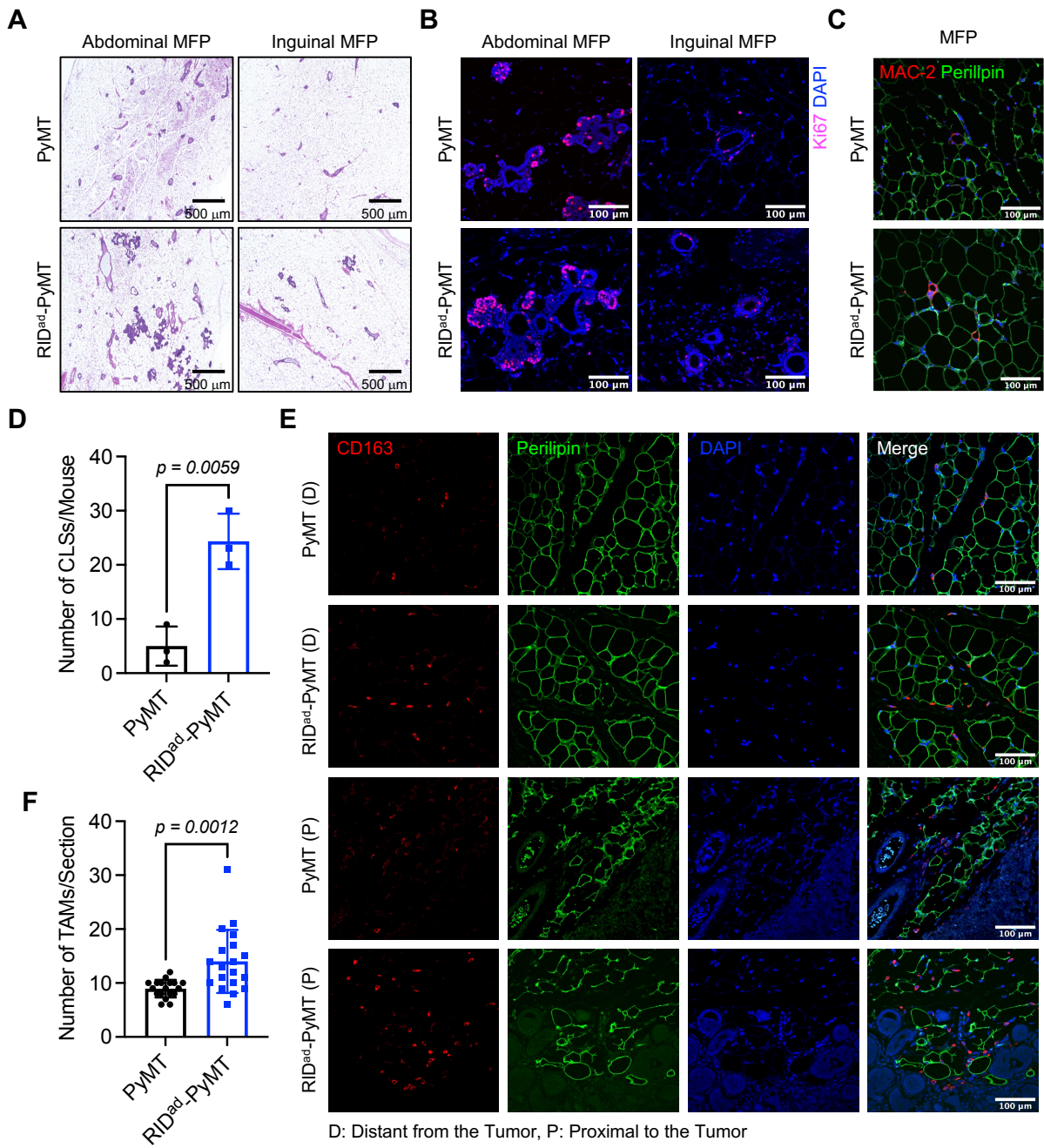
Figure 5 – Kim et al. (2025)



1070

1075

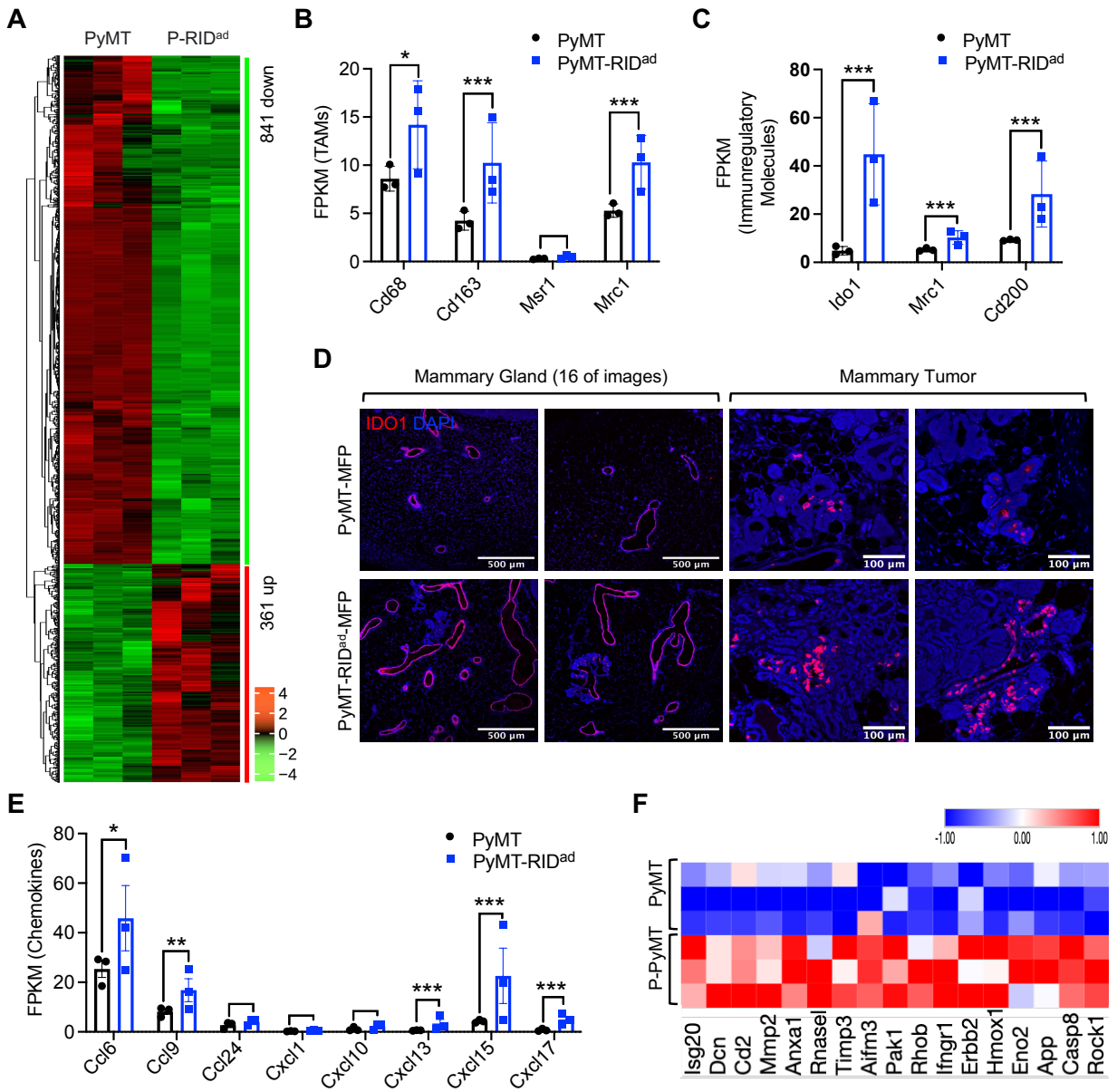
Figure 6 – Kim et al. (2025)



1080

1085

Figure 7 – Kim et al. (2025)



1090

1095

1100

Figure 8 – Kim et al. (2025)

